Structure of thinned continental crust across the Orphan Basin from a dense wide-angle seismic profile and gravity data

K.W. Helen Lau,[1,2] Louise Watremez,[2,*] Keith E. Louden[2] and Mladen R. Nedimović[1]

[1]*Department of Earth Sciences, Dalhousie University, Halifax, NS, Canada. E-mail: kwhlau@dal.ca*
[2]*Department of Oceanography, Dalhousie University, Halifax, NS, Canada*

SUMMARY

We present a 500-km long, 2-D *P*-wave velocity model across the Orphan Basin, offshore NE Newfoundland, Canada, from Flemish Cap to the Bonavista Platform, formed using refraction and wide-angle reflection data from 89 ocean-bottom seismometers. This layered model builds on a recent traveltime tomography result using additional constraints from coincident multichannel seismic reflection and gravity data plus borehole logs from three wells. The model shows (i) post-rift Tertiary (velocities $\sim$1.7–3.5 km s^{-1}) and (ii) both post-rift and syn-rift, Cretaceous and Jurassic sediments ($\sim$4–5 km s^{-1}), deposited within an eastern and a western sub-basin that are separated by a major basement block. The existence of Jurassic sediments indicates a pre-Cretaceous rifting phase in the eastern sub-basin, and possibly in the western sub-basin. However, there is no evidence that Triassic sediments are widespread across the Orphan Basin. Two upper crustal sublayers and one lower crustal layer are defined by differences in velocities (5.4–6.1, 6.1–6.5 and 6.3–7.1 km s^{-1}, respectively) and vertical velocity gradients (mean = 0.14, 0.10 and 0.05 s^{-1}, respectively). Crustal thinning is asymmetric across the Orphan Basin. Within the eastern sub-basin, continental crust beneath Flemish Cap ($\sim$32 km thick; $\beta \sim 1.1$) thins westward into a 35-km-wide zone of hyperextended crust ($<$10 km thick; $\beta > 3.4$) beneath an 11-km-deep sedimentary basin. Within the western sub-basin, the Bonavista Platform crust ($\sim$32 km thick) thins eastward into a 116-km-wide zone of hyperextended crust. Two zones of thicker crust ($\beta = 2$–3.5) exist within the central section, with muted topography within the eastern part and large basement highs in the western part, separated by the eastward dipping White Sail Fault (WSF). The zone to the east of the WSF displays higher velocities in the lower crust than to the west. This can only be explained by a lateral ductile flow across the zone boundary. By combining the two upper crustal sublayers into one, we define the full crustal thicknesses of the upper and lower crusts as 12 and 22 km, respectively. The extension and thinning factors of these two layers are calculated across the basin. Discrepancies between upper crustal thinning and lower crustal thinning are common but only produce a small mass deficit ($\sim$7 per cent or 1.5 km) in the lower crust. Structural connections are shown between the Rockall Trough and the West Orphan Basin and between the Porcupine Basin and the East Orphan Basin in that a wider hyperextended western basin is paired with a narrower eastern basin by a middle zone of thicker crust. In contrast to the Rockall Trough and the Porcupine Basin, serpentinized mantle is not observed in the East Orphan Basin where hyperextended crust is observed ($\beta_{\max} \sim 8.5$). One possible cause is that the restricted size of the basin and its location adjacent to Flemish Cap may have permitted a heavier supply of sediment to cover the basement early during its extension. Such a cover would inhibit the flow of water into the crust and thus leave the mantle unchanged.

Key words: Controlled source seismology; Continental margins: divergent; Continental tectonics: extensional; Crustal structure; North America.

*Now at: Ocean and Earth Science, National Oceanography Centre Southampton, University of Southampton, European Way, Southampton SO14 3ZH, United Kingdom.

1 INTRODUCTION

Many studies of rifted continental margins systematically show that the amount of upper crustal extension is smaller than the bulk thinning of the crust and lithospheric mantle (Driscoll & Karner 1998; Davis & Kusznir 2004). However, how extension is balanced throughout the lithosphere during this depth-dependent stretching (DDS) is not well understood. Thus, observations of thinning at different crustal depths are crucial for understanding the mechanisms that control the formation of rifted margins (e.g. White & McKenzie 1988; Kusznir & Karner 2007). Such constraints have been determined primarily using multichannel seismic (MCS) reflection profiles and wells. The resulting crustal sections can constrain variations in the brittle upper crustal extension from the geometry of faults and variations in syn-rift and post-rift sediment fill. Bulk thinning of the entire crust can be observed by interpreted Moho reflections together with wide-angle refractions where available, with additional constraints from gravity modelling; while thinning of the lithosphere can be deduced from the distribution and amplitude of the post-rift subsidence.

Reston (2009) argues that the amount of upper crustal thinning as determined by measuring the heaves on the faults may have large errors. Alternatively, Reston (2009) used crustal models constrained primarily by wide-angle seismic refraction velocity models in quantifying thinning at different crustal levels. Using a compilation of velocity models across conjugate margins in the North Atlantic, he concluded that the averaged results do not indicate the existence of DDS, conflicting with previous studies. However, the margins that were studied are located mainly in regions characterized by a narrow, rapidly shallowing Moho, with extensional ratios of 20–60 per cent, followed by wide regions with highly thinned crust (>80 per cent). Under these conditions, seismic arrivals in the mid-to-lower crust are not observed over a significant horizontal distance. This problem is exacerbated with wide receiver station spacing, which is generally the case for the existing profiles. Thus, the resulting models derived from these data are not well-constrained for these layers and, therefore, may not adequately characterize how the crust thins over these ranges of extensional ratios.

To improve the constraint of the above analysis, it is necessary to obtain data from basins with a wide zone of extended crust where improved resolution is possible, particularly using refraction data with dense receiver spacing. Orphan Basin, a large, deep water basin located to the east of Newfoundland and northwest of Flemish Cap (Fig. 1), is one of these basins. This basin comprises a particularly wide region of continental rifting (Enachescu *et al.* 2005) that provides an excellent opportunity to study the character of continental crustal deformation under varying degrees of extension. A grid of long, 2-D MCS profiles has recently been collected across the Orphan Basin (Enachescu *et al.* 2005), and one previous long wide-angle profile was taken across the basin along an earlier MCS profile (Fig. 1). However, this profile was acquired in a direction oblique or parallel to the main structural trends and with a resolution that is limited by a wide receiver spacing (Keen & Barrett 1981; Chian *et al.* 2001). Earlier MCS profiles also do not provide good constraints on the depth of basement and Moho, primarily because Moho reflections are often not well imaged (Gouiza *et al.* 2015). Similarly, while gravity helps to define bulk crustal thinning, it cannot adequately give details of intracrustal layering and relief (e.g. Welford *et al.* 2012). Without a well-resolved image of the crust and mantle, the relationships between the shallow and the deeper structures are only speculative, as are the relative thicknesses of upper and lower crust and Moho topography.

Here, we present results using combined dense refraction/wide-angle reflection and deep near-incident seismic reflection data for detailed imaging of the crustal structure across Orphan Basin on a 500-km long 2-D profile (Fig. 1). The refraction/wide-angle reflection data are from a newly collected dense ocean bottom seismometer (OBS) profile oriented approximately perpendicular to major structural trends within the Orphan Basin (Fig. 1). We build a layered velocity model using the RAYINVR algorithm (Zelt & Smith 1992) that allows for abrupt velocity contrasts and is based on traveltime picks of both refracted and reflected arrivals. A smooth and less complex tomographic velocity model, based on first arrivals and Moho reflections (Watremez *et al.* 2015), is used as a starting model, and additional structural constraints are extracted from a coincident MCS profile. Finally, we use the new layered velocity model to develop a better understanding of the crustal response to rifting within the Orphan Basin. In particular, we quantify the lateral variation of crustal thickness; investigate whether DDS and crustal mass imbalance are observed with improved resolutions; and conduct a regional crustal/subcrustal model comparison between Orphan Basin and its European counterpart, namely the Rockall Trough (Morewood *et al.* 2005) and the Porcupine Basin (O'Reilly *et al.* 2006).

2 GEOLOGICAL BACKGROUND

The Orphan Basin is bounded to the north by the Charlie-Gibbs Fracture Zone and its landward extension, the Dover Fault, and to the west by the Bonavista Fault. To the south, the basin joins across the Cumberland Belt Transform Zone with the Jeanne d'Arc and Flemish Pass basins beneath the northeastern Grand Banks. Rifting began at or before the Late Jurassic based on age constraints from deep-water wells (e.g. Blue H-28, Great Barasway F-66 and Lona O-55; Ford & Johnston 2003) and seismic interpretation of Triassic sediments (Chian *et al.* 2001; Enachescu *et al.* 2005). A compilation of basement depths (Louden *et al.* 2004) shows the White Sail Fault (WSF), together with a system of prominent NE–SW trending ridges to its west, divides the basin into a generally shallower eastern, and deeper western, sub-basins (Fig. 1). This difference in basement depths and the role of the WSF in the development of the basin are not well-understood and the deposition of a much thicker Neogene sedimentary layer within the western sub-basin (e.g. at borehole Blue H-28) may alone have caused the asymmetry.

A plate reconstruction at the time of magnetic anomaly M0 time (Srivastava & Verhoef 1992; Skogseid 2010) indicates that the western and eastern Orphan basins and Orphan Knoll form a multibasin rift system that is conjugate to another set of structures formed by the Rockall Trough, Porcupine Bank and Porcupine Basin on the Irish side of the Atlantic. This suggests that early rifting and basin development prior to crustal breakup and the onset of seafloor spreading was complex. The earlier pre-rift position of Flemish Cap is more speculative, but an anticlockwise rotation of this rift-resistant block back into the Orphan Basin has been proposed to avoid an overlap between Flemish Cap and Galicia Bank, while closing the Newfoundland Basin-Iberia gap at pre-M0 times (Sibuet *et al.* 2007). Such an interpretation suggests that the northwestern Flemish Cap and the Bonavista Platform are conjugate sides of the basin.

Rifting within the Orphan Basin has been described using a large set of MCS reflection profiles (Enachescu *et al.* 2005). Fig. 2 shows line drawing of one of the main MCS profiles (Or0–122), which crosses the basin along the direction of extension (Fig. 1). Interpretation from Enachescu *et al.* (2005) is given in Fig. 2 superimposed
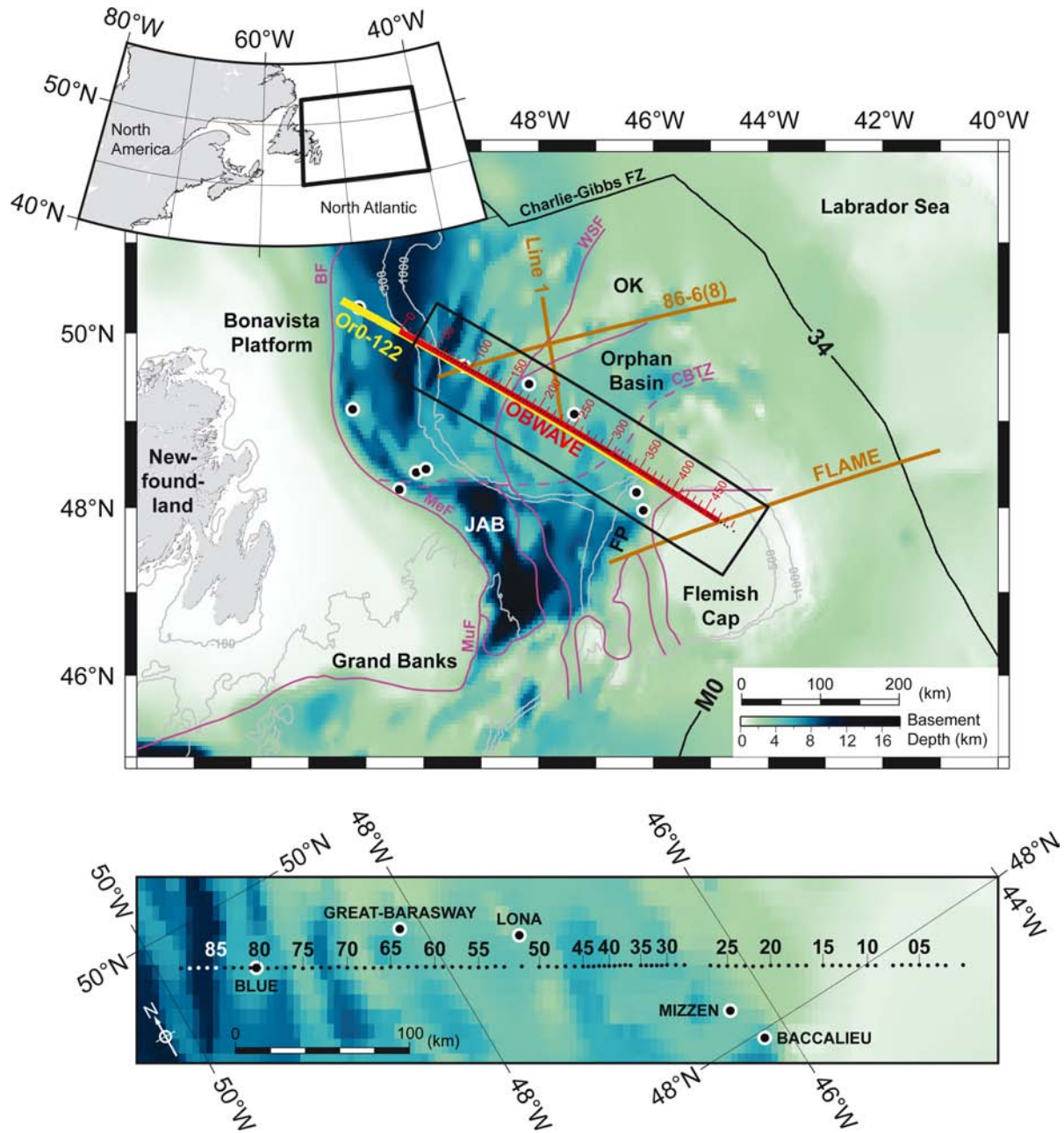
Figure 1. Location of the OBWAVE profile (this paper), coincident MCS profile Or0–122 and previous wide-angle seismic profiles, FLAME (Gerlings *et al.* 2011), 86-6(8) (Chian *et al.* 2001) and Line 1 (Keen & Barrett 1981), and selected boreholes (black filled circle with white outline). Inset shows the location of the study area relative to eastern Canada. Background shows the basement depth (Louden *et al.* 2004) in colour scale and bathymetry with depth contours 100, 500 and 1000 m. Purple lines are faults defined by Enachescu *et al.* (2005). Black lines are magnetic anomalies and fracture zones. Model distances are in red with labelled numbers. Thick red line is the shot line. Small black filled circles are locations of OBSs. Black rectangle shows detailed area plotted in the lower panel with OBSs numbered in black (white where background is dark). OK, Orphan Knoll; JAB, Jeanne d'Arc Basin; FP, Flemish Pass; BF, Bonavista Fault; WSF, White Sail Fault; MuF, Murre Fault; MeF, Mercury Fault; CBTZ, Cumberland Belt Transform Zone; FZ, Fracture Zone.

on this image. The Central Orphan High, which is composed of three major basement highs (70–160 km distances) bounded in the east by the White Sail Fault, divides the basin into eastern and western sub-basins (Enachescu *et al.* 2005). In the East Orphan Basin (Fig. 2a), the Palaeozoic basement was initially rifted at or before the Late Jurassic (Ford & Johnston 2003; Enachescu *et al.* 2005), forming fault blocks observable beneath the eastern end of the profile, although the deepest blocks are not well imaged. The top of the syn-rift Jurassic sediment can be traced across the sub-basin and it shows evidence for perturbation during the second phase of rifting

(Early Cretaceous). The Cretaceous sedimentary layer is relatively more laminated in the upper part and perturbed in the lower part. The Base Tertiary (BT) boundary is a prominent, post-rift basin-wide reflector (Enachescu *et al.* 2005) implying a strong velocity contrast across the boundary that usually represents an unconformity. The Jurassic and the Cretaceous layers are disconnected between the East and the West Orphan Basins by three basement highs, making their interpretations in the West Orphan Basin unconstrained due to the lack of well data. Although the basement depth in the West Orphan Basin is comparable with that of Jeanne d'Arc Basin (Fig. 1;
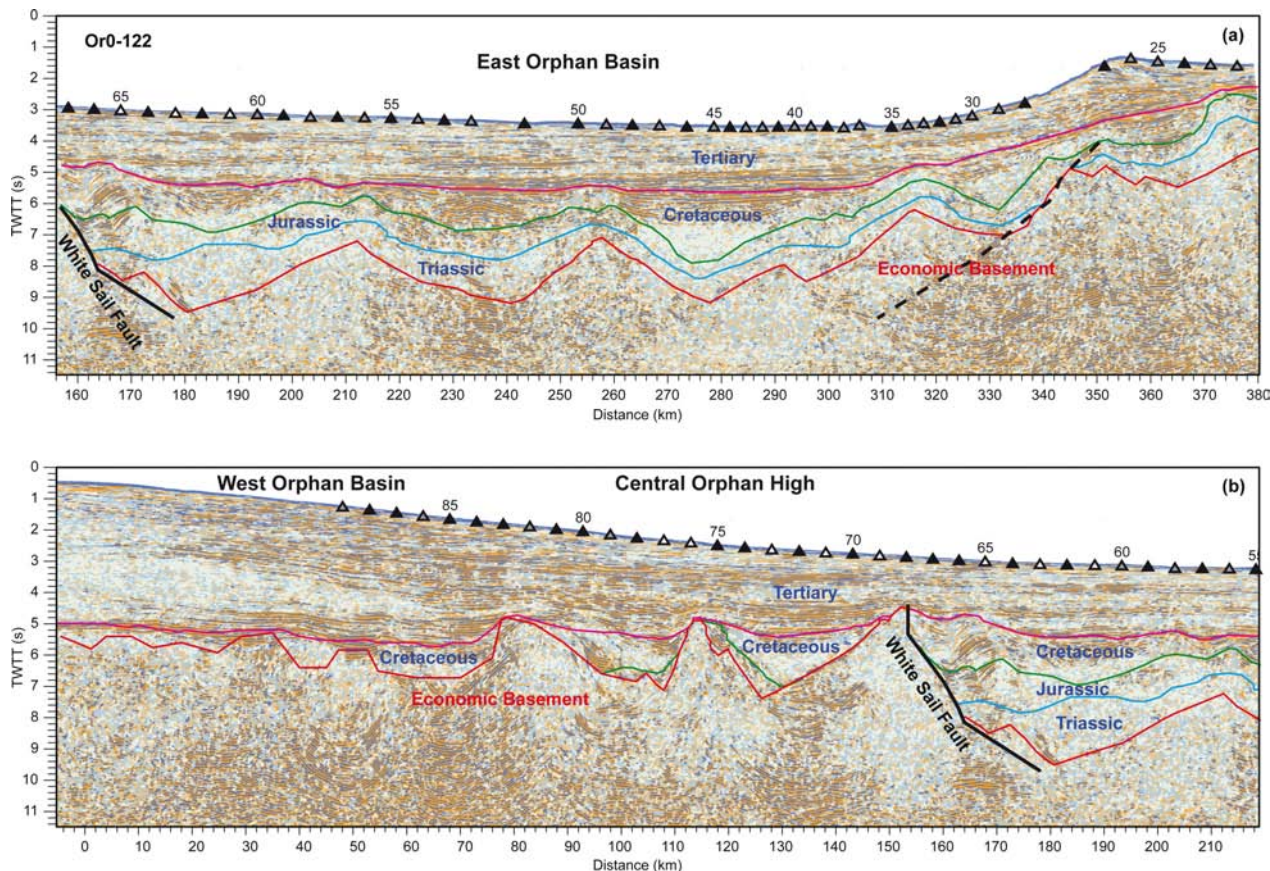
Figure 2. Line drawing of the time migrated section of MCS profile Or0–122 (acquired in 2000 by Geophysical Services Incorporated and scanned from paper copy provided by the Canada-Newfoundland Offshore Petroleum Board). This profile is spatially coincident with the OBWAVE wide-angle OBS data coverage. Colour solid curves represent horizons interpreted by Enachescu *et al.* (2005). Black lines are interpreted faults. Triangles are OBS locations with filled colours representing differing constraints input to the model: black, fully picked; grey, partially picked; white, only first-arrival picked; unfilled, no picks.

Watremez *et al.* 2015), no Jurassic sediments have been observed in shallower wells near the Bonavista Fault, suggesting that the basin may not have opened until the second phase of rifting in the Early Cretaceous. However, this can also be a result of the lack of wells that are deep enough to penetrate into potential Jurassic sediment. Profile Or0–122 extends further into the West Orphan Basin for another 80 km, but it is not covered by our wide-angle seismic data.

The top of the crystalline basement has been difficult to define without coincident seismic velocity constraints from wide-angle seismic data. Instead, an economic basement top is determined as the lower bound of petroleum interest (Enachescu *et al.* 2005). A crustal model from gravity inversion (Welford *et al.* 2012) shows rapid crustal thinning from a ~17-km-thick crust to the thinnest crust (~7 km thickness) at distances 280–300 km within the East Orphan Basin. The Moho in the Central Orphan High and the West Orphan Basin is less well-defined (Fig. 2b). Chian *et al.* (2001) model gravity data to extend their velocity model (86–6(8); Fig. 1) into the West Orphan Basin. Their model shows full-thickness crust beneath the Bonavista platform that thins rapidly seawards of the Bonavista Fault with a 100-km wide region of very thin crust (5–13 km thick) beneath the deepest basement. Welford *et al.* (2012) show similar results.

3 WIDE-ANGLE SEISMIC DATA

Wide-angle data along a 500-km long 2-D profile were collected in 2010 during the OBWAVE (Orphan Basin Wide Angle Velocity Experiment) program. This profile, which extends from northwestern Flemish Cap to the western Orphan Basin, is approximately orthogonal to the overall strike of primary rifted structures within the basin (SW–NE; Fig. 1). Its location was chosen to be coincident with MCS profile Or0–122, acquired in 2000 by Geophysical Services Incorporated (Fig. 2). Wide-angle data with an 8-ms sample rate were retrieved from 89, four-component OBS receivers positioned 3–5 km apart. An array of nine airguns (total volume = 75.5 L) was shot at a 60-s interval, giving an average source spacing of 140 m. Further details regarding data acquisition, instrument relocation and data preconditioning to form receiver gathers are given in Watremez *et al.* (2015).

The OBS data were plotted as common receiver gathers and picked for coherent compressional wave events corresponding to reflections and refractions (diving waves) through various seismic layers (Figs 3–8). Unfiltered data were used as much as possible and, in other cases, only Butterworth bandpass filtering and/or predictive deconvolution were applied. Hence, OBS data were picked using different processed versions of the same data, optimized for the different phases. Since Watremez *et al.* (2015) already described the first arrivals and Moho reflection, the discussion here is focused on secondary arrivals not already discussed.

Clear refracted and reflected *P*-wave arrivals from the shallow sediments (layers S1–S4; Table 1 and Fig. 3) are mainly observed as later arrivals. Phases from these layers are consistently observed throughout the profile, except for the eastern end where the layers pinch-out onto Flemish Cap. For OBS 48 (Fig. 3), the apparent
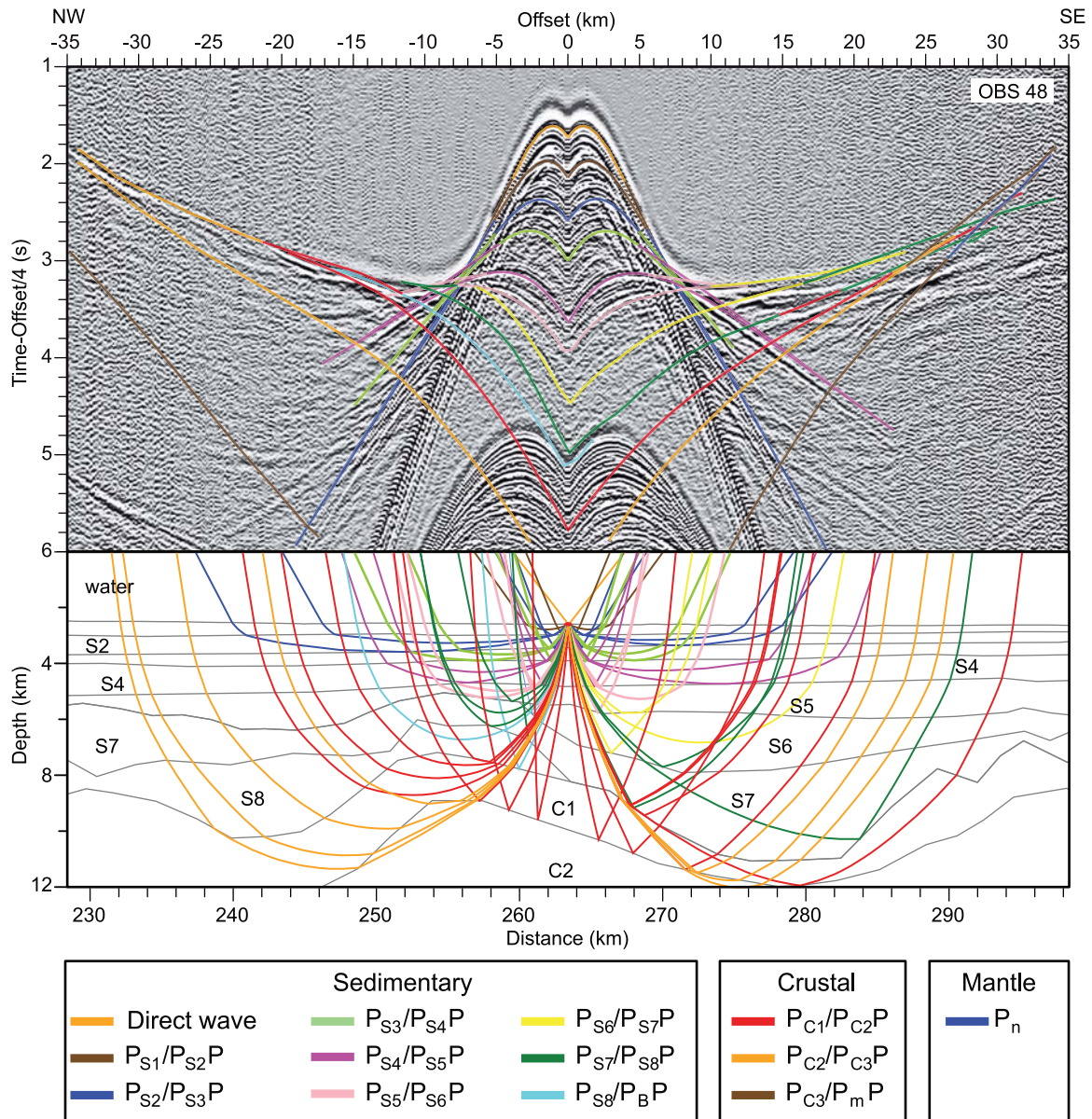
Figure 3. Forward velocity modelling for OBS 48. Top: hydrophone data overlaid by theoretical traveltimes versus model distances from ray tracing through the final velocity model. Traveltime is reduced by 4 km s^{-1} relative to shot-receiver offsets. The data have been processed with zero-phase predictive deconvolution and bandpass filtering. Bottom: the corresponding ray-path diagram. Grey lines are model boundaries. See legend for colour coding of phases. S1–S8 are sedimentary layers; C1 and C2 are upper crustal layers; C3 is lower crustal layer. See Table 1 for nomenclature of observed phases.

velocities are significantly slower (i.e. dipping downwards) than the reduction velocity of the plot (4 km s^{-1}). The reflection boundary ($P_{S5}P$) is consistently the strongest sedimentary reflection observed, in agreement with a significant increase in the apparent velocity for the underlying sediments (S5–S8). The deeper sedimentary layers are constrained primarily by first arrival phases with apparent velocities of 4 km s^{-1} or greater (i.e. dipping upwards). Reflections from these layers (e.g. $P_{S6}P$) are also observed that further constrain their velocities and layer depths.

Figs 4–8 display data over a larger offset range with a reduction velocity of 6 or 7 km s^{-1} to show more clearly the crustal (C1–C3) and mantle arrivals. These five OBS records are selected to show important constraints on the variations in these deeper arrivals along the profile. For clarity, phases of the sedimentary layers are simplified into a single colour.

Starting from the eastern end of the profile, OBS 18 (Fig. 4) represents constraints for the thick Flemish Cap continental crust, which thins to the west as indicated by the asymmetry of the data on opposite sides of the OBS. The observations of two major mid-crustal reflections ($P_{C2}P$ and $P_{C3}P$) suggest the existence of a three-layered crust (see also Fig. A1). The refracted P_{C3} phase consists typically of secondary arrivals, especially for the deepest rays. The Moho depths are partially constrained by the wide angle Moho reflection (P_mP). Its amplitude is very strong at far offsets (-100 to -50 km), which is a common observation on the better quality OBS data (Figs 4–8). This indicates that the velocity contrast across the Moho is large and sharp. The amplitude of P_mP decreases as it approaches vertical incidence. However, for instruments that have high signal-to-noise ratios, such as OBS 18, P_mP arrivals can be observed from large offsets to 10 km (Fig. A1). The P_n phase constrains mantle velocities as
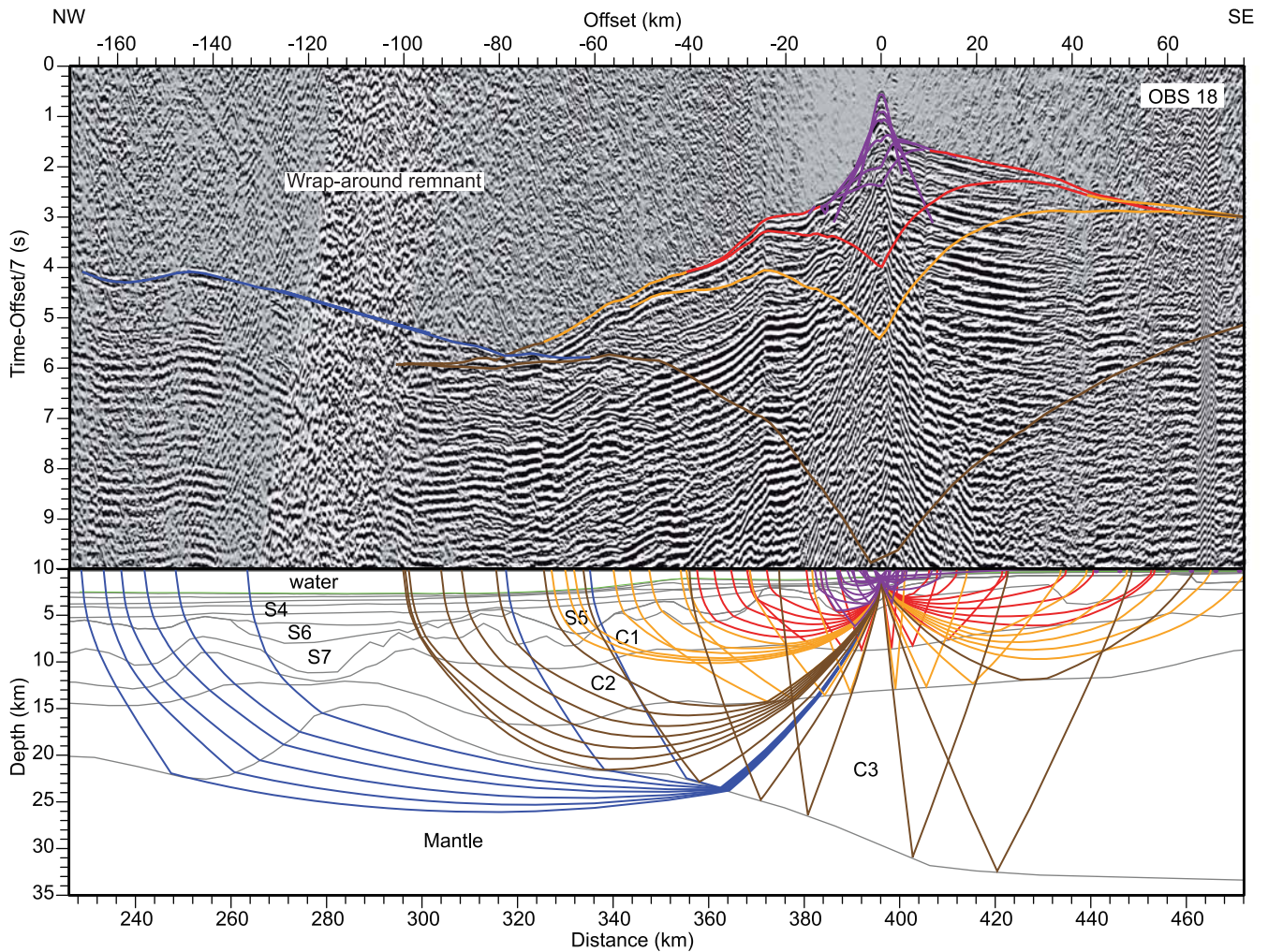
Figure 4. Forward velocity modelling for OBS 18. Top: vertical geophone data overlaid by theoretical traveltimes versus model distances from ray tracing through the final velocity model. Traveltime is reduced by 7 km s^{-1} relative to shot-receiver offsets. The data have been processed with minimum phase bandpass filtering, trace interpolation and dip filtering to enhance deep crustal and mantle signals and to attenuate the wrap-around noise. Bottom: the corresponding ray-path diagram. See Fig. 3 caption for explanations of additional figure components.

well as Moho depths. Its apparent velocity is much higher than the reduction velocity (7 km s^{-1}) and the apparent velocity of P$_{C3}$. At larger offsets, its arrivals are often difficult to pick due to both weak amplitude and overprinting by coherent wrap-around (i.e. previous shot) noise. Therefore, more advanced processing was undertaken to reduce this noise (Fig. 4; see Watremez *et al.* 2015 for details). Note, however, that the effect of this processing produces additional artefacts such as the amplification of coherent noise other than the wrap-around noise (compare Fig. 4 with Figs 5–8). Therefore, these sections are only used for picking the P$_n$ phase.

Further west along the profile at OBS 38 (Fig. 5), asymmetry is again observed in the data. First arrival phases indicate a major deepening in basement topography. For later arrivals, we observed good P$_{C2}$P reflections to constrain the thinning of layer C1 towards the west. Furthermore, the crossover between the P$_m$P and P$_{C3}$ phases occurs at a smaller offset ($\sim$−35 km) on the western side than the eastern side ($\sim$84 km), indicating a very thin crust in the immediate west of the OBS. The much shallower Moho is also constrained by the first arrival P$_n$ phase. The symmetry in crustal phases changes to the west at OBS 53 (Fig. 6). The observed symmetry and the average apparent velocity of $\sim$6 km s^{-1} for first arrival phases from the crust indicate relatively uniform basement topography. The symmetry in

later phases, P$_{C2}$P and P$_{C3}$, also indicates relatively horizontal mid-crustal boundaries. The crossover between P$_m$P and P$_{C3}$ arrivals at a larger offset ($\sim$60 km) suggests a deeper Moho compared to the western side of OBS 38 (distance 290 km).

At OBS 67, further to the west, significant asymmetry is again observed in all sub-basement phases (Fig. 7), indicating that basement is generally much shallower to the immediate west. This asymmetry is most significant for layer C3, with the P$_{C3}$ phase appearing as a weak first arrival to the west and as strong second arrivals to the east. This observation indicates two very different lower crustal velocity structures across the two sides of the OBS. The crust on the western side is situated beneath the three major basement highs observed in the MCS profile (Fig. 2; distance 70–160 km). OBS 67 also shows very clear P$_{C2}$P and P$_{C3}$P reflections on the eastern side, constraining depths for the mid-crustal boundaries in the three-layered crustal model. The quality of the P$_m$P arrivals is outstanding for this OBS, providing excellent constrains on the deepening of Moho to the west.

Finally near the western end of the profile, OBS 87 (Fig. 8) is located on the western side of the three basement highs. The P$_{C3}$P reflections observed on both sides of the OBS constrain the westward tilting of the top boundary for layer C3. The observed
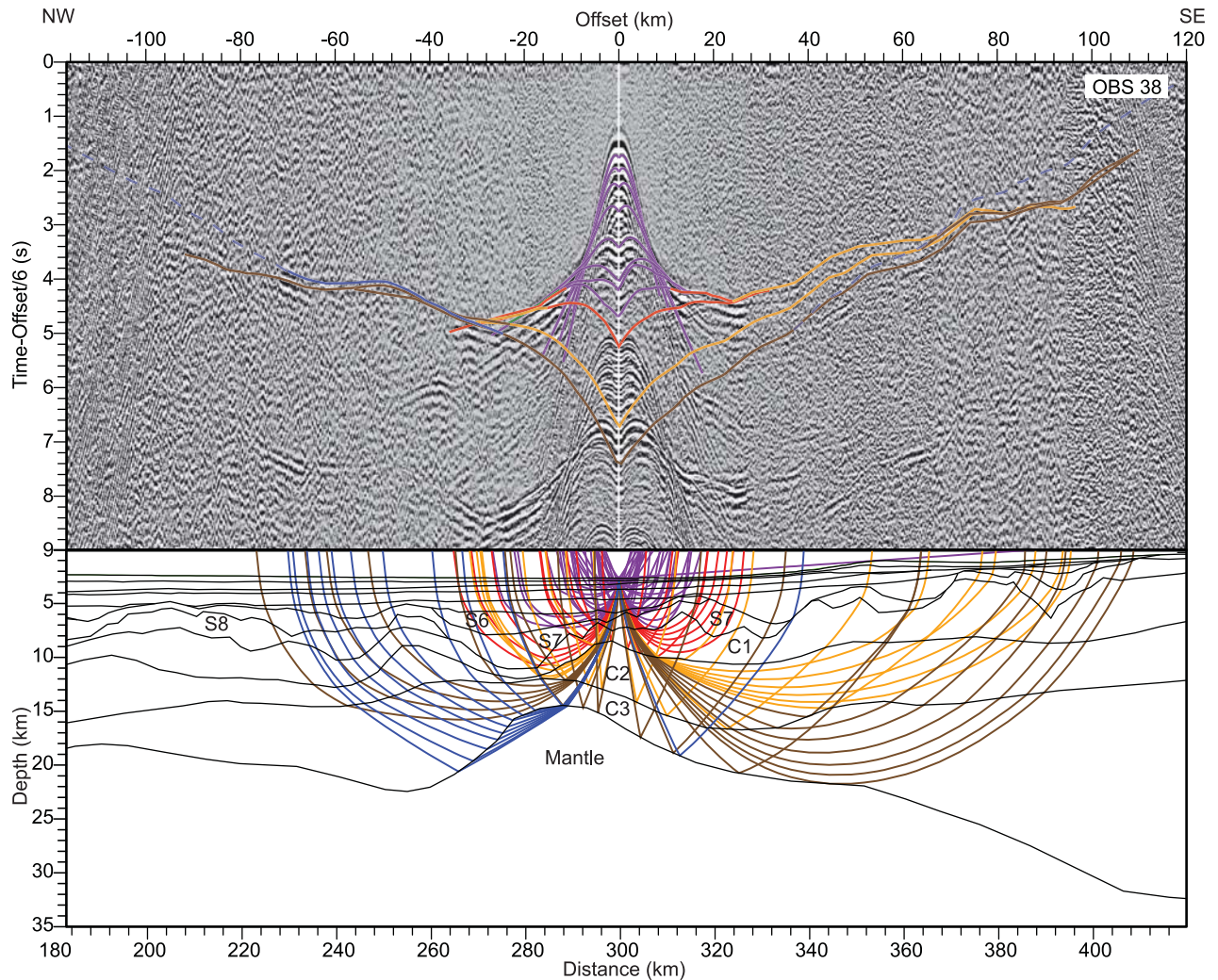
Figure 5. Forward velocity modelling for OBS 38. Top: hydrophone data overlaid by theoretical traveltimes versus model distances from ray tracing through the final velocity model. Traveltime is reduced by 6 km s^{-1} relative to shot-receiver offsets. The data have been processed with zero-phase bandpass filtering to enhance deep crustal signals. Bottom: the corresponding ray-path diagram. See Fig. 3 caption for explanations of additional figure components.

crustal phases on the eastern side are similar to those on the western side of OBS 67, except that P$_m$P is less strong, indicating a weaker velocity contrast across the Moho. Here, the crossover point of the P$_n$ phase provides an additional constraint to Moho depths.

4 SEISMIC MODELLING

4.1 Methodology

We used the program RAYINVR (Zelt & Smith 1992), a ray-tracing modelling algorithm using layers parameterized by top and bottom depth and velocity nodes, to produce a *P*-wave velocity model to fit the observed traveltimes layer-by-layer. The water layer, for simplicity, is assigned a constant velocity of 1.5 km s^{-1} and seafloor depths were converted from echo soundings (in two-way traveltime) along the profile. Reflection traveltimes from a coincident, migrated MCS profile Or0–122 (Fig. 2) were used jointly with OBS observations to constrain the depths of all layer boundaries. Observed phase arrival times initially were fit visually by comparing ray-traced traveltime curves with the data for the purpose of phase identification from top to bottom layers (Figs 3–8). Velocities from the earlier Tomo2D tomography model (Watremez *et al.* 2015) were used as a reference.

Once a preliminary model was produced, we hand-picked selected phases with pick uncertainties assigned manually according to our confidence in the pick depending on the signal frequencies and the signal-to-noise ratios (Table 2). Arrivals are picked at the first zero-crossing of the wave. Inversion was then performed using these picks to optimize the model fit. Since we observe phases from up to 13 layers, we picked all the observed phases only on OBS stations with good data quality and at approximately even spacing along the profile (black filled triangles; Fig. 9). To improve the resolution for some parts of the model, some additional stations were partially picked only for deeper sedimentary layers and upper/middle crustal layers (grey filled triangles; Fig. 9). For the remaining stations, we used the first arrival picks from Watremez *et al.* (2015). Picks were subsequently decimated to a minimum of 100 m spacing to prevent the inversion and error analysis from over emphasizing regions with close trace spacing.

4.2 *P*-wave velocity model

Fig. 9(a) shows the final *P*-wave velocity model from which 1-D profiles are extracted in Figs 10 and 11 to show details at key locations. According to the velocity structure, layers S1–S8 are interpreted as
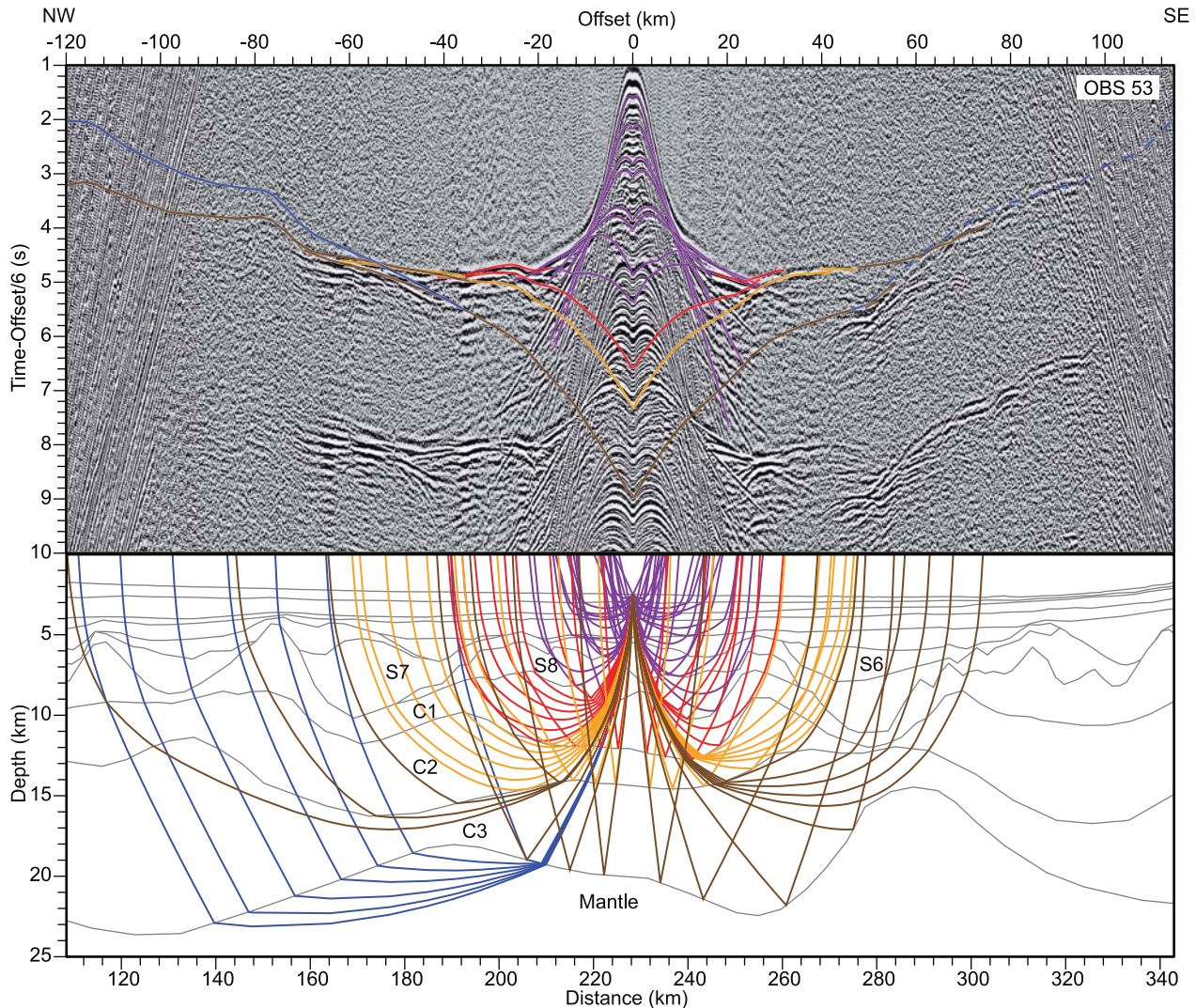
Figure 6. Forward velocity modelling for OBS 53. Top: hydrophone data overlaid by theoretical traveltimes versus model distances from ray tracing through the final velocity model. Traveltime is reduced by 6 km s^{-1} relative to shot-receiver offsets. The data have been processed with zero-phase bandpass filtering and deconvolution to enhance deep crustal signals. Bottom: the corresponding ray-path diagram. See Fig. 3 caption for explanations of additional figure components.

sedimentary (Fig. 10) and layers C1–C3 as crustal. The modelled sedimentary velocities agree very well with check shot data from Great Barasway F-66 (Fig. 10b) although it is ~22 km away from the profile. According to the Blue H-28 and Lona O-55 wells (Figs 10a and c), layers S1–S4 are equivalent to the Tertiary post-rift sequence (Enachescu *et al.* 2005) with velocities of ~1.7–3.5 km s^{-1}. These layers extend throughout the basin, gradually thickening into the West Orphan Basin (Fig. 9a). Layers S5–S8 represent another distinctive assemblage of sediment whose velocities are ~4–5 km s^{-1} with exceptionally high velocities of >5 km s^{-1} at the base of the deep basins (e.g. 285 km). Furthermore, their boundaries are more undulating than for shallower sedimentary layers with many pinch outs at structural highs. Note that although layer S8 shares the same velocity range as layer S7, at locations where both layers exist (190–270 km), the former is a distinctive layer in which velocities are higher than in the overlying layer (Figs 10c and 11d).

Layers C1, C2 and C3 are three relatively thick layers (average thicknesses are 3, 4 and 11 km, respectively) representing crustal velocities of different velocity gradients: high in layer C1 (mean = 0.14 s^{-1}), medium in layer C2 (mean = 0.10 s^{-1}) and

low in layer C3 (mean = 0.05 s^{-1}). A similar three-layered crust in the region is also reported by Chian *et al.* (2001) and Gerlings *et al.* (2011). As these layers change along the profile, four distinctive zones (Zones 1–4; Fig. 9a) can be defined that display unique characters in their velocities and thicknesses. Note that these profile zones are not divided by sharp boundaries, especially between Zones 1 and 2. Here, the decreased resolution within thin crustal layers (see Section 4.3) leads to uncertainty in the extent of this boundary which is thus shown to extend over a broad area hereafter called the boundary zone that is marked by the dashed lines in Fig. 9(a).

Zone 1 (distances 300–500 km; Figs 9a and 11f), the easternmost zone, shows a typical rifted margin structure where unstretched continental crust (~32 km thick) in the east thins westwards to near rupture within a boundary zone to the west. Fault block structures as inferred from topography are seen in layer C1 with a velocity of 5.4–6.1 km s^{-1} except at 320 km distance where the velocity at the top becomes as low as 5.0 km s^{-1}. Layer C2 has a velocity of 6.1–6.5 km s^{-1} with only slight changes in thickness until distance 300 km, before thinning to nearly break up within the boundary zone.
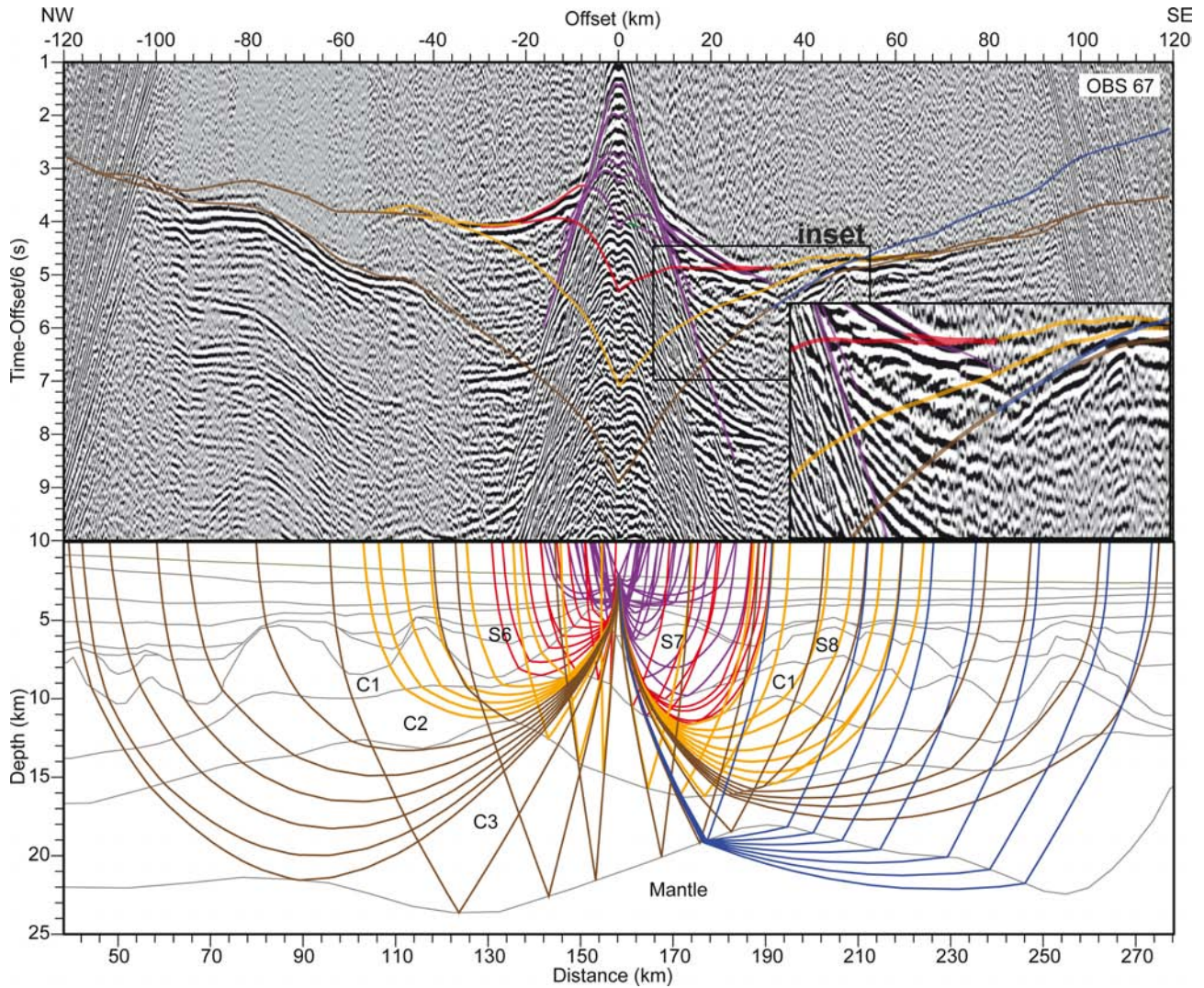
Figure 7. Forward velocity modelling for OBS 67. Top: vertical geophone data overlaid by theoretical traveltimes versus model distances from ray tracing through the final velocity model. Traveltime is reduced by 6 km s^{-1} relative to shot-receiver offsets. The data have been processed with zero-phase bandpass filtering and deconvolution to enhance very low frequency (4–8 Hz) signals. Black rectangle shows the detailed area plotted in the inset. Bottom: the corresponding ray-path diagram. See Fig. 3 caption for explanations of additional figure components.

In contrast, thinning in layer C3 (6.3–7.1 km s^{-1} in velocity) spans a wider distance: initially by thinning moderately from 25 to 18 km thickness east of model distance 410 km, but then thinning rapidly to <3 km thickness over a distance of 120 km into the boundary zone. Note that the location of maximum thinning in layer C3 is offset to the east by ∼10 km from maximum thinning of layers C1 and C2.

Zone 2 (Figs 9a and 11d) is delimited by two major basins, one centred on the boundary zone at 270–300 km (Fig. 11e) and the other at 180 km (Fig. 11c). In Zone 2, only layers C1 and C2 are symmetrical in velocity structure to those of Zone 1 on the other side of the boundary zone. In contrast, the velocities within layer C3 are higher at the same depths beneath the C2/C3 boundary than in its surrounding zones (c.f. Figs 11b, d and f). The velocity gradient in layer C3 (0.03 s^{-1}) is also lower than in Zone 1 (0.1 s^{-1}) with similar thicknesses.

Zone 3 (Figs 9a and 11b) contains three basement highs observed at 70–180 km distances. The crust as a whole thickens towards the middle of this zone. Note that the velocity contours for 6.7–6.9 km s^{-1} dip eastwards instead of following the Moho as in

Zone 1. This causes a region of very low velocity gradient (0.01 s^{-1}) in the eastern half of this zone and a large velocity contrast across the Moho (Fig. 11c). Otherwise, the velocities of the three crustal layers are similar to Zone 1. Note that the truncation of iso-velocity contours by the Moho is observed within both Zones 2 and 3.

Zone 4 (Figs 9a and 11a) extends to the west of the three basement highs further into the western Orphan Basin. The crust is thinner than to the east. Although the velocities within layer C3 in Zone 4 are continuous with those of Zone 3, the velocity range of 6.5–6.7 km s^{-1} is missing in the former, creating a velocity discontinuity at the C2/C3 boundary similar to layer C3 in Zone 2. Finally, the mantle velocity is modelled to be 8.0 km s^{-1} or above underneath the entire layer C3. Fig. 11 shows good large-scale agreement between the RAYINVR layer velocity model and the final Tomo2D velocity model (Watremez *et al.* 2015). Detailed differences in some layers result from the methodology by which velocity structures are parameterized in the two models: RAYINVR uses a set of discrete linear velocity trends within each modelled layer while Tomo2D uses a grid of a smoothed velocity field. For instance, shallow sedimentary layers are primarily determined in the layer model by secondary
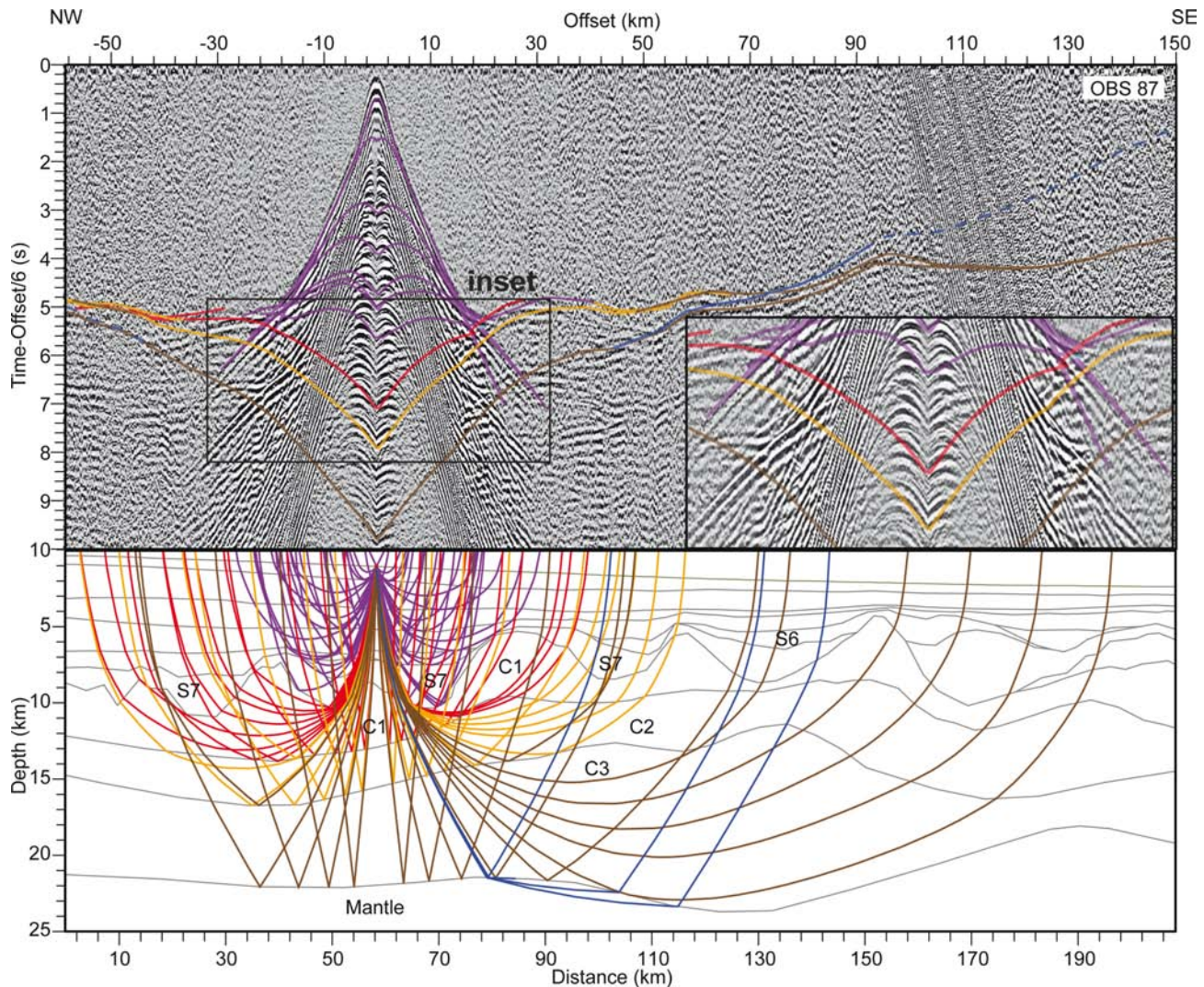
Figure 8. Forward velocity modelling for OBS 87. Top: hydrophone data overlaid by theoretical traveltimes versus model distances from ray tracing through the final velocity model. Traveltime is reduced by 6 km s^{-1} relative to shot-receiver offsets. The data have been processed with zero-phase bandpass filtering to enhance deep crustal signals. Black rectangle shows the detailed area plotted in the inset. Bottom: the corresponding ray-path diagram. See Fig. 3 caption for explanations of additional figure components.

arrivals due to their low velocities relative to deeper layers. These arrivals are not considered by the Tomo2D inversion as they are not first arrivals and can only be interpreted from changes in gradient (e.g. corresponding to layer S7). Therefore, tracing unconformities within the sediment, such as the BT boundary, is best done using a layer model. A similar problem exists for the interpretation of top basement (top of C1; Fig. 11).

While the velocities for C1 are very similar in both models, the velocities above C1 tend to be overestimated in the Tomo2D model due to smoothing. Finally, a major difference occurs in layer C3, where the RAYINVR model indicates both lower velocities and gradients, unlike the Tomo2D model, except within the boundary zone between Zones 1 and 2 (Fig. 11e). By assuming a smooth velocity transition across the Moho boundary, the Tomo2D inversion overestimates the lowermost crustal velocities while underestimating uppermost mantle velocities. Such smoothing tends to create artefacts in the lower crust and upper mantle that can be mistaken as underplate and/or serpentinized mantle. On the other hand, by assuming a single sharp contrast at the boundary, the RAYINVR model can also simplify what is likely to be a more complex reality,

as suggested by the strong but yet complex nature of the observed P_mP arrivals (e.g. Fig. 6). Thus, both models have their limitations that only approximate the 'true' velocity structure.

4.3 Error analysis and resolution for velocity model

Root-mean-square (rms) residuals t_{rms} (0.127 s overall) and normalized χ^2 (0.719 overall), with respect to pick uncertainties of ∼5–400 ms, were calculated for all picks by two-point ray tracing. Table 2 shows that although some phases are fit better than others, all phases have $\chi^2 \leq 1$, meaning that the model fits the observation within picking uncertainties, except for P_{S1} and P_{C1}. The larger χ^2 value for P_{S1} (3.102) is caused by the inclusion of two high-gradient sedimentary layers into one due to their small thicknesses and by the low values of pick uncertainties (average of 20 ms) due to the high signal-to-noise ratio of the arrivals. The fact that subsequent sedimentary layers S2–S8 all have low χ^2 values indicates that misfit to the initial layer has not affected the accuracy in the underlying structure. The relatively high χ^2 for P_{C1} (1.294) indicates that

Table 1. Glossary of seismic phases.

Phase	Description
Direct	Direct wave through the water
P_{Sn}	*P*-wave refracted phase through the *n*th sedimentary layer from the top
$P_{Sn}P$	*P*-wave reflected phase from the top of the *n*th sedimentary layer from the top
$P_{S5}P$	*P*-wave reflected phase coincident with Base Tertiary unconformity
$P_{S8}P/P_BP$	*P*-wave reflected phase from the basement top
$P_{C1}/P_{C2}/P_{C3}$	*P*-wave refracted phase through the crystalline crustal sublayers 1/2/3
$P_{C2}P/P_{C3}P$	*P*-wave reflected phase from the top of the crystalline crustal sublayers 2/3
P_mP	*P*-wave Moho reflection or reflection at the crust-mantle boundary
P_n	*P*-wave refracted phase through mantle

the basement topography is too complex to allow for complete ray tracing in some parts of the model. In this case, the inversion is unable to improve the fit without losing too many arrivals. The basement layer should thus be considered as an approximation to a more complex structure. Note that the smaller OBS spacing in this experiment, with much improved coverage from overlapping diving rays, has allowed us to define a more complex basement structure than would be possible in standard surveys. The low χ^2 values for the underlying crustal and mantle layers also indicate that unresolved basement structure has not degraded the underlying model.

The model resolution for different parts of the model is indicated by the diagonal values of the resolution matrix (Zelt & Smith 1992) for each velocity node (Fig. 9b). Model regions with resolution >0.5 are considered well resolved and those with resolution <0.3 are considered poorly resolved. The number of picks and their distribution in relation to the structures control this value. Fig. 9b shows good resolution (>0.5) in most parts of the model. The resolution is very good (>0.7) in the Tertiary sequence (S1–S4) except for the two ends of the model where overlapping rays are absent. For layers S5–S8, we have good resolution (>0.5) within deep and wide basins, such as distances 160–180, 270–300, 325–350 and 430–460 km. Our crustal velocities are very well resolved (>0.7) for Zone 3 and the thick crust (distances 410–450 km) in Zone 1. Layer C3 is well resolved except for the region with a steeply dipping Moho, which limits the number of diving rays (Fig. 5). The mantle velocities are very well constrained (>0.8) throughout the model. Poorly resolved (<0.3) regions are limited to layers with high-velocity gradients and small thicknesses, and for layers that pinch out (e.g. the structural high at 260 km distance and the crust beneath the large basin at 270–290 km distances). Although the resolution can potentially be improved by removing thin layers and pinch-out structures (i.e. by combining layers S7 and S8), we chose to keep them for consistency with MCS observations (Section 6.1). The low resolution (<0.3) in layer S7 at 340–370 km distance and in the underlying upper crust is due to an observational gap between OBS 27 and OBS 28.

Most of the model boundaries are sampled by reflected phases (black lines in Fig. 9b) and have high resolutions (>0.5; Fig. A2). In particular, the Moho (P_mP) is observed along the entire model, except near its ends. The BT discontinuity ($P_{S5}P$) is also very well sampled. While the depths of basement (top of layer C1) are uncertain in the MCS data (Fig. 2), we are able to observe this boundary on

Table 2. Error analysis statistic for picked OBSs: number of ray-traced picks (*n*), mean uncertainty of all input picks ($t_{uncertainty}$), rms residual between modelled and observed traveltimes (t_{rms}) and normalized (χ^2).

	Phase	*n*	Mean $t_{uncertainty}$ (s)	t_{rms} (s)	χ^2
Sediment	P_{S1}	2257	0.022	0.027	3.102
	$P_{S2}P$	1879	0.031	0.018	0.341
	P_{S2}	4354	0.037	0.030	0.762
	$P_{S3}P$	5184	0.043	0.027	0.352
	P_{S3}	2753	0.047	0.025	0.296
	$P_{S4}P$	3579	0.046	0.025	0.248
	P_{S4}	4773	0.053	0.030	0.426
	$P_{S5}P$	6032	0.051	0.032	0.492
	P_{S5}	2100	0.043	0.025	0.457
	$P_{S6}P$	1781	0.059	0.023	0.157
	P_{S6}	1515	0.062	0.034	0.335
	$P_{S7}P$	1579	0.053	0.028	0.315
	P_{S7}	6563	0.059	0.036	0.527
	$P_{S8}P/P_BP$	4262	0.066	0.047	0.474
	P_{S8}	886	0.059	0.043	0.412
	$P_{B'}P$	999	0.064	0.024	0.145
Crust	P_{C1}	18 738	0.098	0.079	1.294
	$P_{C2}P$	8056	0.103	0.102	0.875
	P_{C2}	22 343	0.129	0.104	1.022
	$P_{C3}P$	16 597	0.160	0.118	0.544
	P_{C3}	22 375	0.194	0.140	0.550
	P_mP	34 186	0.232	0.167	0.534
Mantle	P_n	22 041	0.276	0.219	0.847
All		194 832	0.141	0.127	0.719

Note: The basement reflection is comprised of P_BP (reflection from the bottom of S7 where S8 is absent) and $P_{B'}P$ (reflection from the bottom of S8).

wide-angle reflections (Fig. 3), although only sparsely over Flemish Cap. Constraints on sedimentary layers and basement top are particularly reduced for the eastern end of the model, beyond the SE end of the MCS profile (distance >380 km; Fig. 9b).

We have also estimated the uncertainties in the depths of the Moho, the top lower crustal (C3) boundary and the top basement due to their importance for the discussions on DDS. A robust Monte Carlo analysis has already been presented by Watremez *et al.* (2015) for the Tomo2d model to obtain standard deviations of inverted Moho depths under a series of random perturbations to the starting model. Since their Moho reflection picks and velocity model are similar to ours, we use their results as depth uncertainties for our Moho (Fig. A2). This work, however, did not invert the top of the crystalline basement and the top of the lower crustal reflections. Instead, we use sensitive tests to estimate the uncertainties for the depth to the reflection from the upper-to-lower crust boundary. The distance range of 155–220 km was chosen as a representative segment of this boundary and was perturbed vertically from the final model. Fig. A3 shows the increase in χ^2 due to such perturbations after ray tracing for a number of OBSs above the perturbed boundary. The *f*-test showed that any perturbations >±250 m would result in models that are different from the final model at >98 per cent confidence. Such a high confidence is a result of using >7000 picks. Note that the much lower-than-optimal χ^2 of the final model indicates that this segment was better fit than the average of the model as a whole. Since the top basement was primarily defined by the MCS section, we estimated a depth uncertainty of ±50 m using a quarter of the dominant wavelength of the basement reflection.
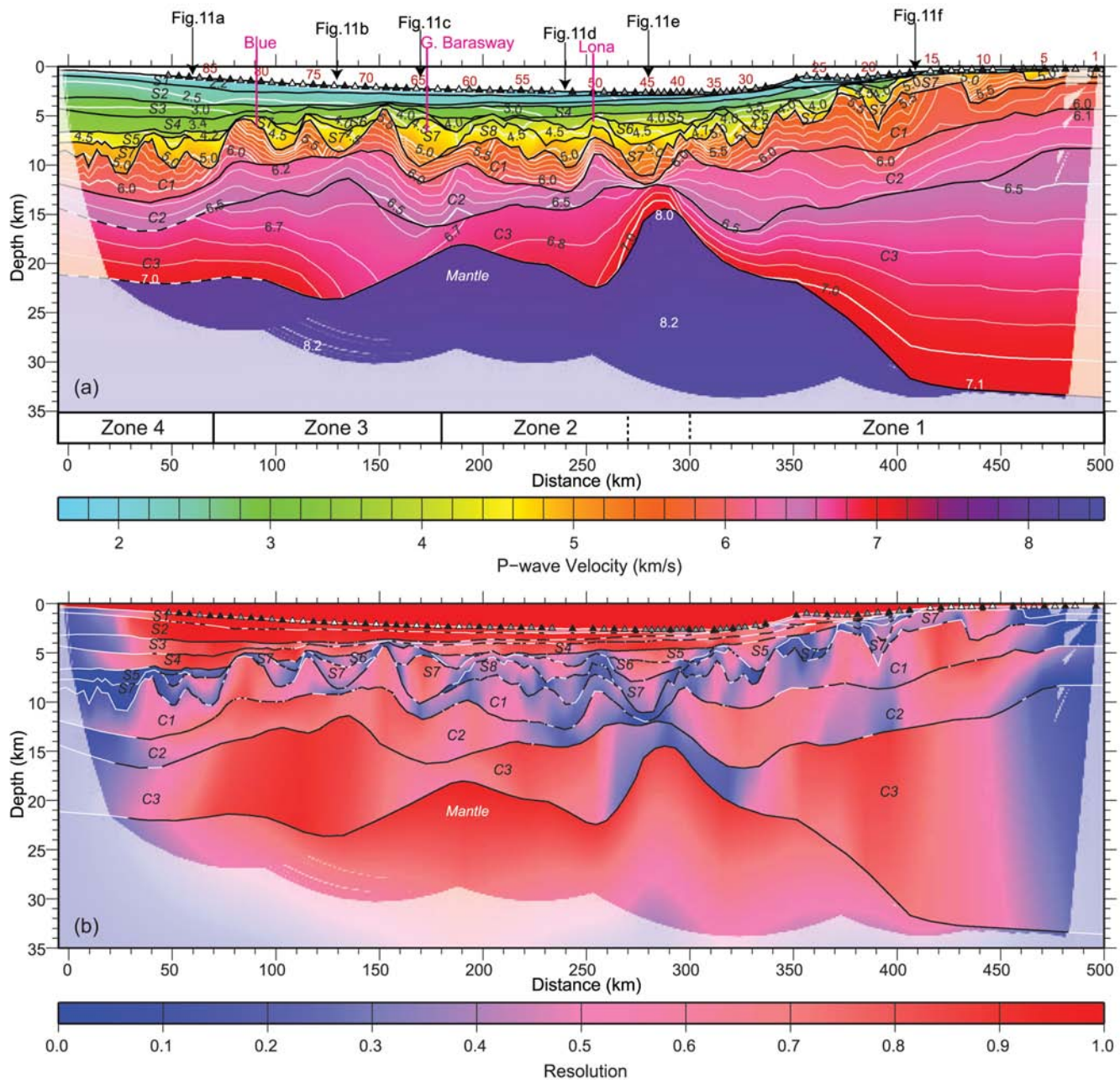
Figure 9. Final *P*-wave velocity model and resolution. See Fig. 2 caption for explanation of OBS colour fills (triangles). Layers are labelled according to Fig. 3 legend and Table 1. Zones 1–4 are zonal interpretation of the crustal velocity structure (see the text). Regions outside ray coverage are masked. (a) Velocity model with layer boundaries in black lines and velocities defined by colour scale. Velocities 1.5–5.0 and 5.0–8.0 km s^{-1} are contoured every 0.5 and 0.1 km s^{-1}, respectively (white lines). OBS numbers are in red; vertical pink lines are well positions projected along profile. Vertical black arrows locate the 1-D velocity–depth profiles plotted in Fig. 11. (b) Model resolution plot. Colour scale shows gridded diagonal values of the resolution matrix for all velocity nodes. Note that values for areas between layer boundaries are linearly interpolated from values along the boundaries. Black lines represent locations of layer boundaries illuminated by picked reflections and white lines are locations without observations.

5 GRAVITY MODELLING

Fig. 12(a) shows the free-air gravity anomaly derived from satellite altimetry (Sandwell & Smith 2009). Orphan Basin is enclosed by large gravity highs that overlie Flemish Cap, the margin of the Bonavista platform and Orphan Knoll. Within the basin, the gravity is characterized by a regional low with local minima and maxima that become more pronounced after removing longer wavelengths (>80 km; Fig. 12b). The filtered data show trends that reflect the local basement and Moho topography, which within the basin are

approximately perpendicular to the OBWAVE profile (Fig. 1). In particular, an elongated gravity high is observed near 290 km model distance that extends from south of Orphan Knoll towards Flemish Pass. East of Orphan Basin, the trends are mainly perpendicular to the direction of the opening of the Atlantic Ocean, as expected for the formation of oceanic crust.

A 2-D gravity model along the OBWAVE profile and extending further onto the Bonavista Platform (Fig. 13) was constructed for two reasons: (1) to check for consistency between the final velocity
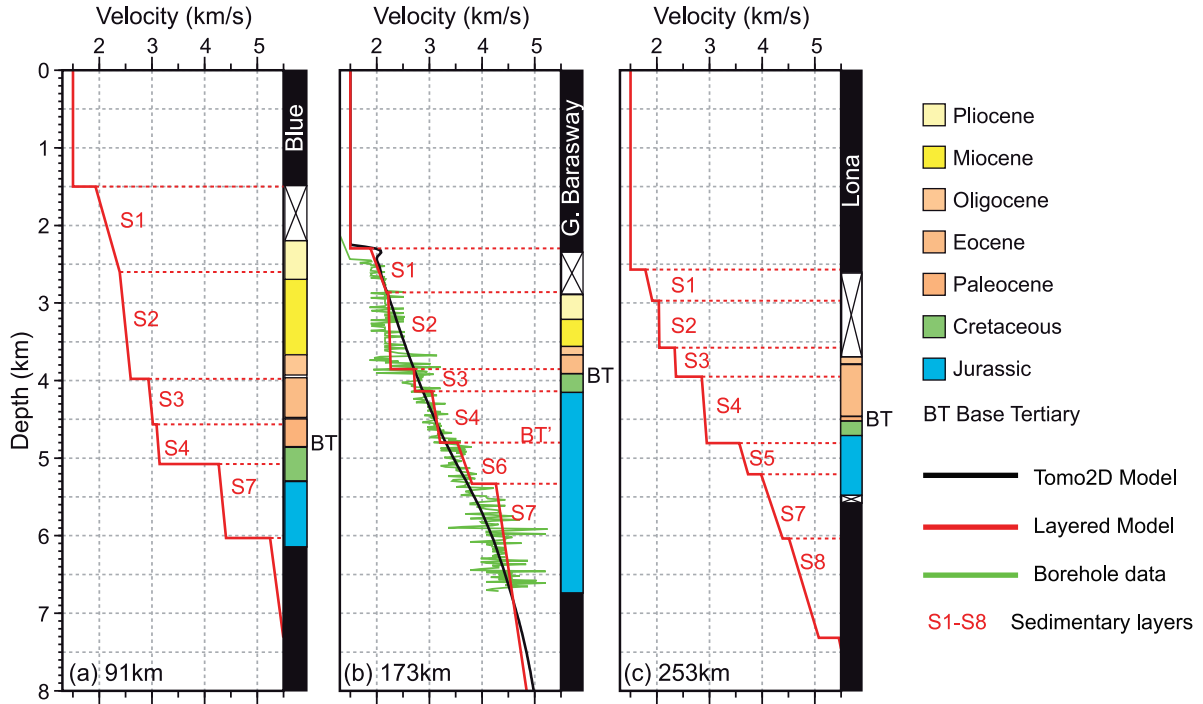
Figure 10. 1-D velocity versus depth profiles through the sedimentary layers of the final model at projected locations of wells (a) Blue H-28, (b) Great Barasway F-66 and (c) Lona O-55. Projections for (b) and (c) are made along structural trends. Ages of stratigraphic units are taken from previous interpretations of well data. Model layer labels are same as in Fig. 9.
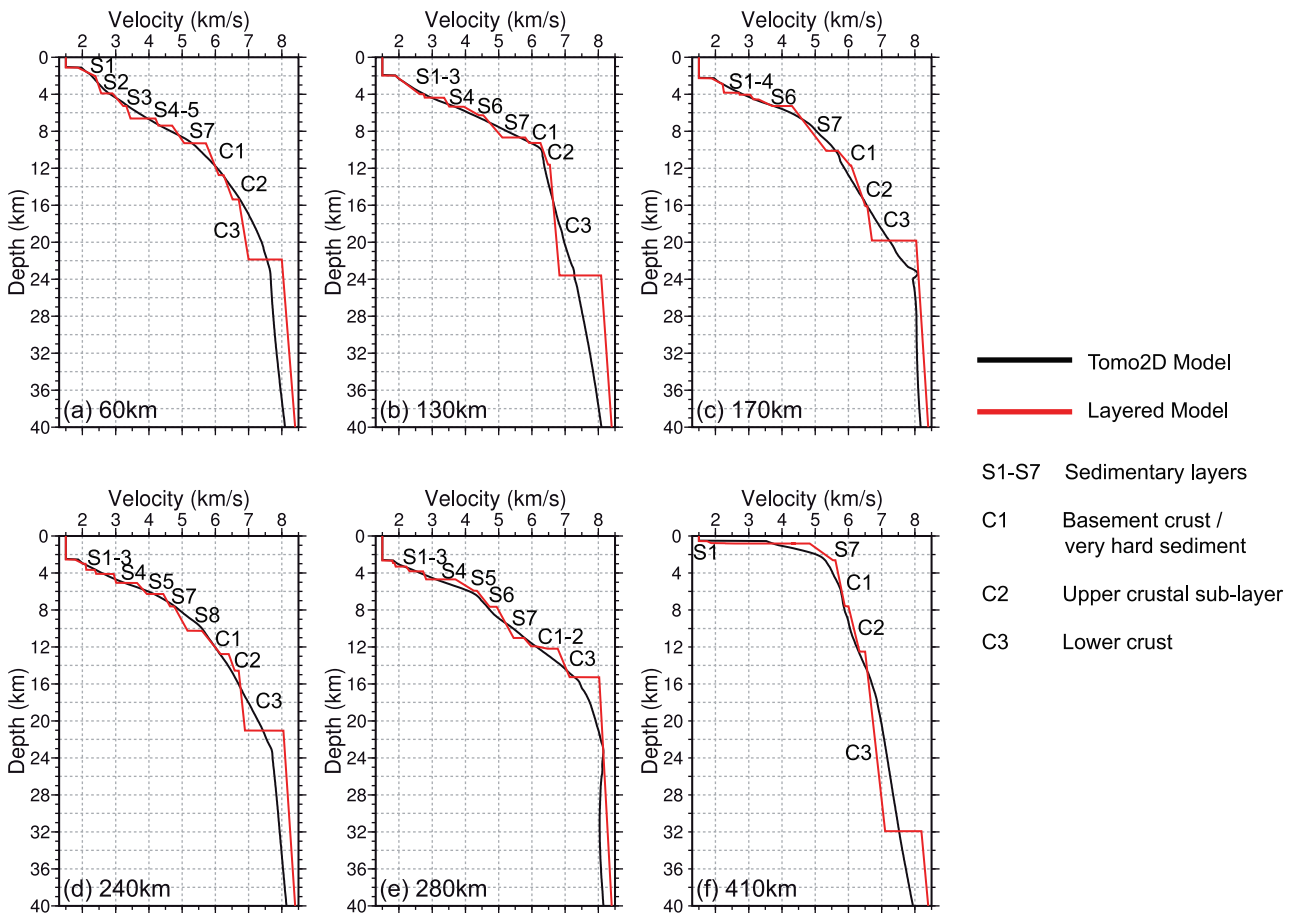

Figure 11. 1-D velocity versus depth profiles extracted at selected locations from the RAYINVR final layered velocity model (red) and the Tomo2D final smooth tomographic velocity model (black; Watremez *et al.* 2015). See Fig. 9(a) for locations on the 2-D profile.
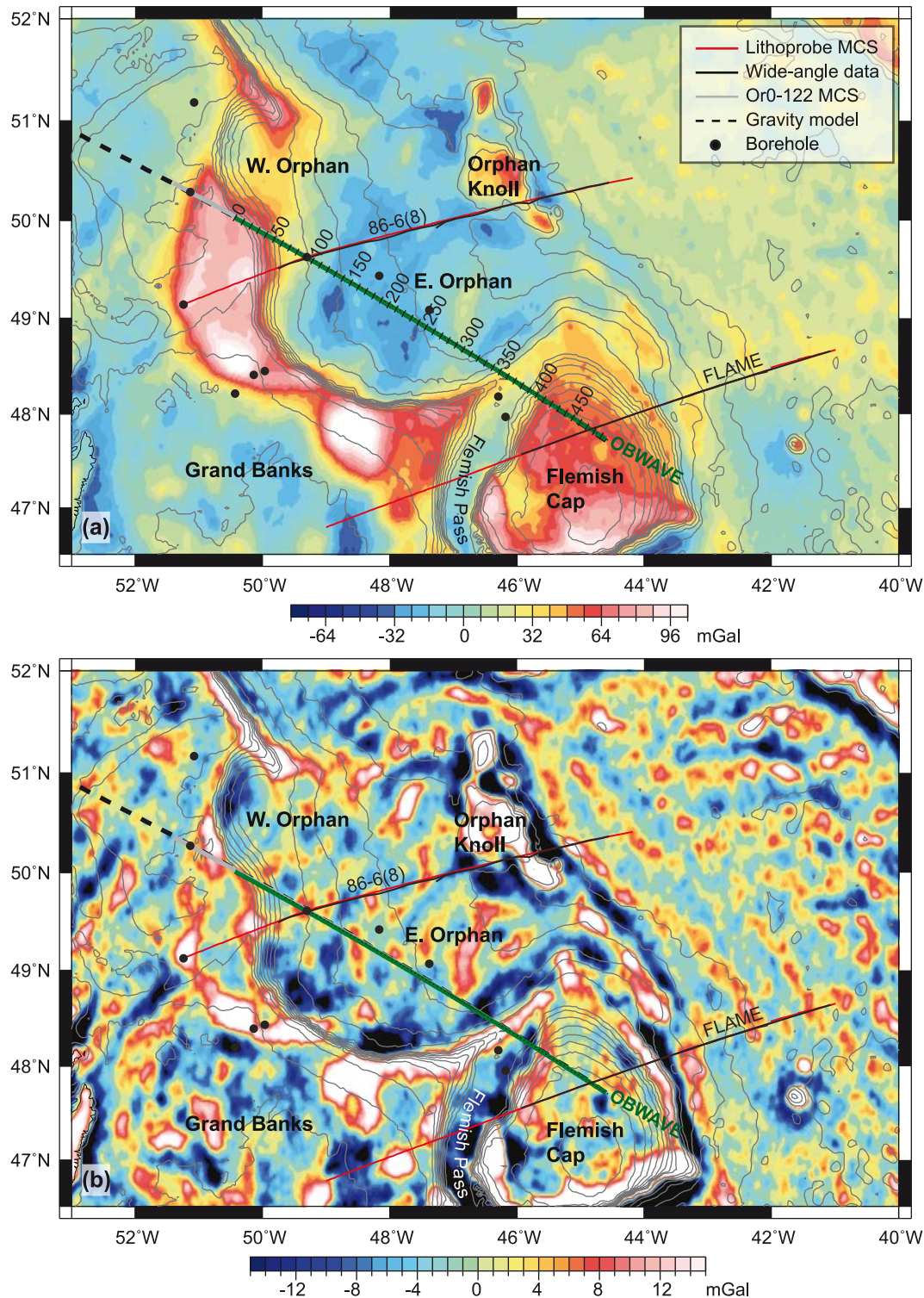
Figure 12. Observed gravity over the study area. The gravity model shown in Fig. 13 extends along the OBWAVE profile (dark green line; this paper), the western continuation of the MCS profile Or0–122 (thick grey line) and a further extension to the west (black dashed line). Grey contours are bathymetry. (a) Free-air gravity anomaly (FAA) and colour scale (Sandwell & Smith 2009) with locations of relevant profiles (see inset legend). (b) Same as (a) but the FAA has been filtered to keep only short wavelength components (<80 km) to highlight basement structures.

model and the observed gravity and (2) to extend the structural model further to the northwest beyond the OBWAVE profile for constructing a complete cross section of the basin (Fig. 12). Given the lateral consistency of the filtered gravity, a 2-D model of the gravity should be a reasonable approximation for a scale of at least

100 km out of plane from the OBWAVE profile. The observed free-air gravity anomaly along the model profile (Fig. 13a) was modelled using the methodology of Talwani *et al.* (1959) and Won & Bevis (1987). A density model is approximated by simplifying the final velocity model into major layers, assigning a representative velocity
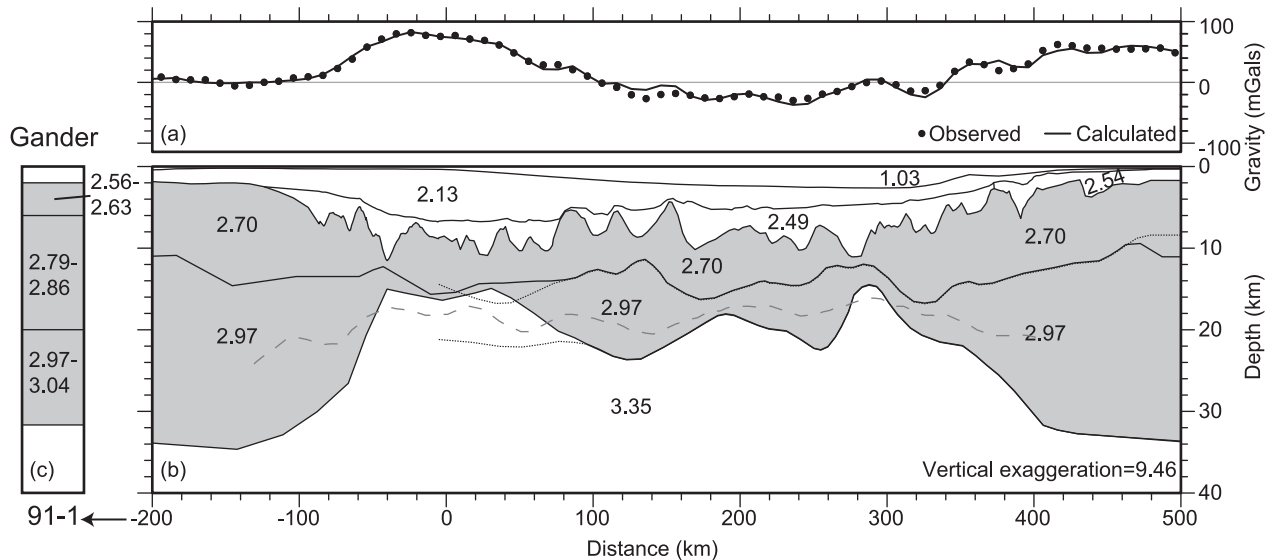
Figure 13. Density model (Mg m^{-3}) derived from the final velocity model. Modifications of the mid-crustal boundary and Moho are necessary for distances −5–50 km to fit the gravity. Forward gravity modelling was performed to extend our velocity model further westward to cover the entire rift. (a) Observed (Sandwell & Smith 2009) and calculated gravity anomalies from (b) the 2-D density model. Dashed grey line is the Moho according to a 3-D gravity inversion (Welford *et al.* 2012). Dotted black lines are layered velocity model mid-crustal and Moho boundaries. (c) Density model derived from the wide-angle *P*-wave velocity model of the Gander crust along LITHOPROBE 91–1 (Chian *et al.* 1998), which intersects with the projected western end of the density model.

for each layer and converting it into density using the relationship given in Lau *et al.* (2006). For the western extension of the profile beyond the velocity model, we picked the sediment and basement horizons based on the time-migrated section of Or0–122 up to its termination at −90 km model distance. For model distances beyond the MCS profile (i.e. −200 to −90 km), basement depths were extracted from the 2-D grid shown in Fig. 1 (Louden *et al.* 2004). The mid-crustal and Moho boundaries were extrapolated for model distances beyond the refraction model by the gravity model.

Fig. 13(b) shows the final gravity model with an rms misfit between observed and calculated values of 5.4 mGal. This close agreement indicates that the final velocity model is consistent with the observed gravity. Note that a minor adjustment to the mid crustal boundary at the eastern end (distances 460–500 km) of the velocity model is required to fit the gravity where the seismic constraint is poor (compare Figs 9b and 13b). Furthermore, the mid-crustal and the Moho boundaries for distances −5–50 km have been modified from those of the velocity model to fit the gravity. The cause of this discrepancy may be the lack of resolution in the velocity model (Fig. 9b) or a violation of the 2-D gravity assumption (Fig. 12a) over this part of the model. Nevertheless, the gravity high at distances −60–30 km is consistent with a relatively wide region of very thin crust, similar to the result of Chian *et al.* (2001). The sharp thinning to near rupture at distance −40 km is similar to the models of Chian *et al.* (2001) and Welford *et al.* (2012) to fit the basin bounding gravity high seawards of the Bonavista Fault. For our model, this thinning terminates at distance −140 km with a 32 km thick crust most likely of the Gander terrane at the western end. Our modelled whole crustal thickness (32 km) and the crustal velocities are consistent with that from the LITHOPROBE wide-angle seismic profile 91–1 (Chian *et al.* 1998) further to the west when converted to densities using the same relationship as mentioned above (Fig. 13c). Since our upper crust is equivalent to a combined upper and middle crust in the Chian *et al.* (1998) model, Fig. 13 suggests a thickening of the upper crust and a thinning of the lower crust towards Newfoundland. However, this difference is not a result of rifting

since the total crustal thicknesses of the two models are similar. The gravity model, therefore, provides us a complete cross section of the Orphan Basin rift.

Fig. 13(b) also shows a comparison between our derived Moho and that obtained by Welford *et al.* (2012) using 3-D inversions of gravity data. The later model shows that the Moho, over distances 20–60 km, is ~4 km deeper than in our gravity model and closer to the Moho depth in our velocity model (Fig. 9a). Therefore, 3-D structures may have affected the observed gravity, such that Moho depths from 2-D modelling may have been underestimated. Over the region constrained by our velocity model, the overall shape of the Moho variations is similar between the two models. However, the amplitude of the Moho fluctuations is much less pronounced in the model of Welford *et al.* (2012). This is likely caused by the difference in density models across the Moho. Our model includes a large increase in density at the Moho, consistent with the seismic velocity model, and no sub-Moho contribution to the anomaly. In contrast, the model of Welford *et al.* (2012) is characterized by a vertical density gradient that extends deeper into the mantle, resulting in an underestimation of the amplitude of Moho depth variations. As shown in Fig. 13, this effect can create substantial differences in the degree of crustal thinning predicted by gravity models alone. A detailed calibration between seismic and gravity models is required to reduce these differences. Although not coincident with the present profile, Gouiza *et al.* (2015) shows similar Moho depths as ours along a nearby profile using the same gravity modelling algorithm as in this paper.

6 DISCUSSION

6.1 Comparison to MCS reflection data

We first convert the bitmap image of the time migrated section of Or0–122 (Fig. 2) into depth by vertical stretching using the final RAYINVR velocity model. We then use a combination of the
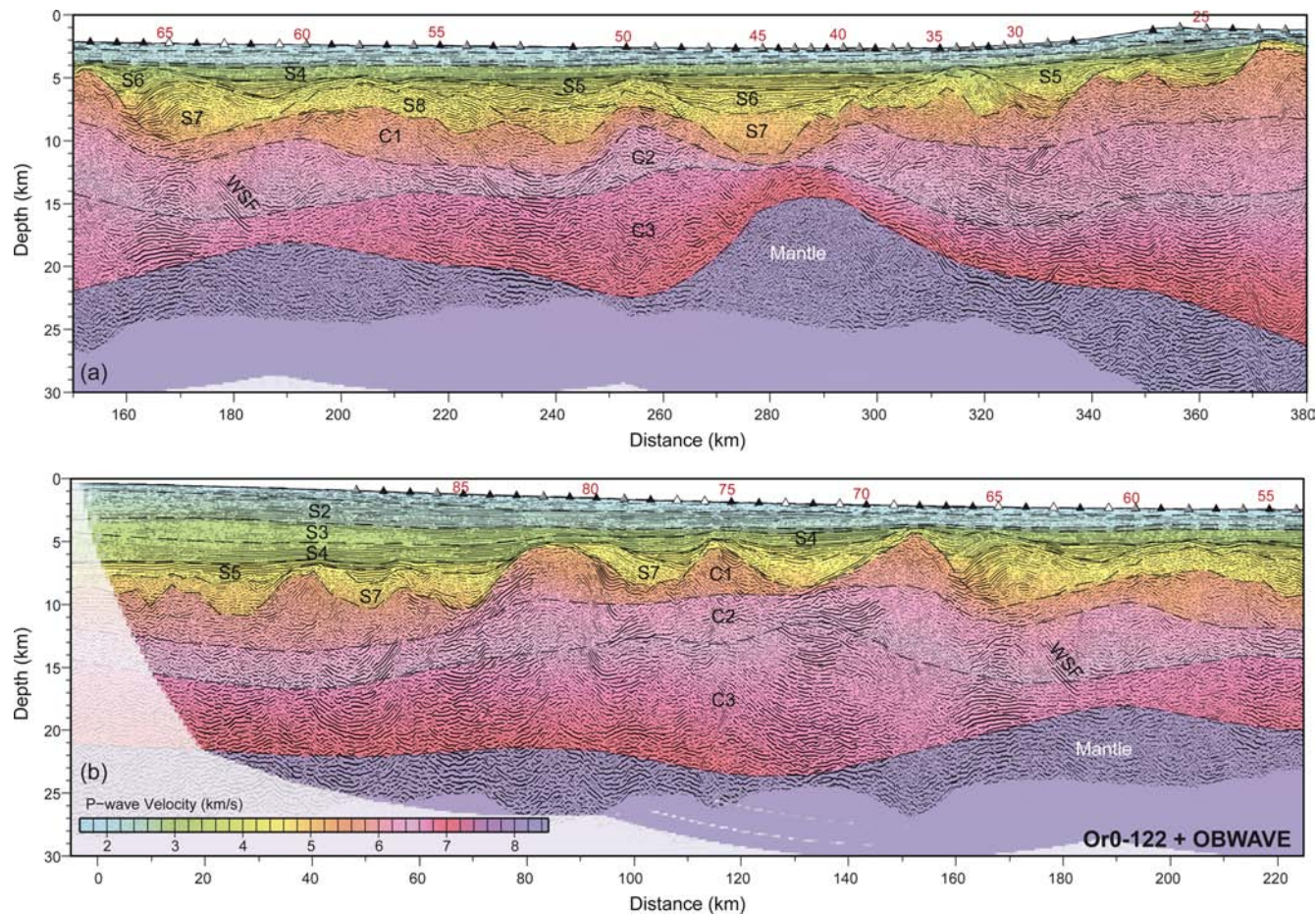
Figure 14. MCS profile Or0–122 (foreground reflectivity) after depth conversion of scanned time section (Fig. 2) using the layered velocity model (colour background). Dashed lines are model boundaries; triangles are OBS positions. See Fig. 9 for explanation to labelling of layers and OBS fill colours. Regions outside ray coverage are masked. WSF, White Sail Fault.

velocity model (Fig. 9a), the depth-converted MCS observations (Fig. 14), well data (Fig. 10) and the gravity model (Fig. 13) to interpret the observed structures (Fig. 15).

Note that while effort has been put to ensure the best consistency between the OBS data and the MCS reflection section when modelling the velocity model boundaries, it was not possible to have perfect correspondence between the two. First, the OBSs often are not exactly located on the plane of the MCS section due to drifting during descent, imaging out-of-plane structures that are potentially different from those on the MCS section. Second, the level of detail in imaged structures is a function of various acquisition parameters including frequency content of airguns, locations of receivers and sources, etc. These parameters are different between the OBS and the MCS data. Furthermore, the MCS section is an image of near-incident reflections, while the OBS velocity model boundaries are based on interpretation of refracted phases according to velocities. If these velocity boundaries coincide with wide-angle reflections, they can sometimes be traced many kilometres back to near incidences but are not always observable due to decreasing amplitude with offsets. They may also be unreflective if they are used as a modelling procedure for changing the velocity gradient, since the RAYINVR velocity model only allows linear velocity changes within layer. Lastly, we also do not expect steeply dipping structures in the MCS section to match those of the velocity model, as the former may not have been correctly depth migrated to the right dip due to errors in velocity constraints.

6.2 Sedimentary section

Three wells (Blue H-28, Great Barasway F-66 and Lona O-55) have been drilled into the deep sediment offset offline by 0, 22 and 16 km, respectively, from the OBWAVE profile (Figs 1 and 9a). Only the Great Barasway well contains check shot data for comparison with our velocity model (Fig. 10b). We do not expect a perfect match between the drilled stratigraphic units (as well as the borehole velocities, where applicable) and our velocity model due to both the differing resolution scales between these investigative approaches and the offset between the well and the seismic profile. However, we do expect that prominent boundaries, such as the BT boundary, to be consistent between the observations. At the Blue and Lona wells (Figs 10a and c), the BT boundary is consistent with the base of layer S4, which is also consistent with a prominent reflector in the MCS data (Figs 2 and 14). At the Great Barasway, although there is a close agreement between check shot data and our velocity model, the stratigraphic BT occurs higher in the section, capping an unusually thick (∼2.5 km) Jurassic section. To reconcile this discrepancy, we propose a new BT boundary at the base of S4 (BT′), such that the Mesozoic layers would have velocities consistently above 3.5 km s^{-1}.

Despite being sampled by a grid of MCS profiles (Enachescu *et al.* 2005), the interpreted ages of the syn-rifted sediment layers in the West Orphan Basin are not constrained due to the lack of deep boreholes in the basin and lack of structural continuity across the
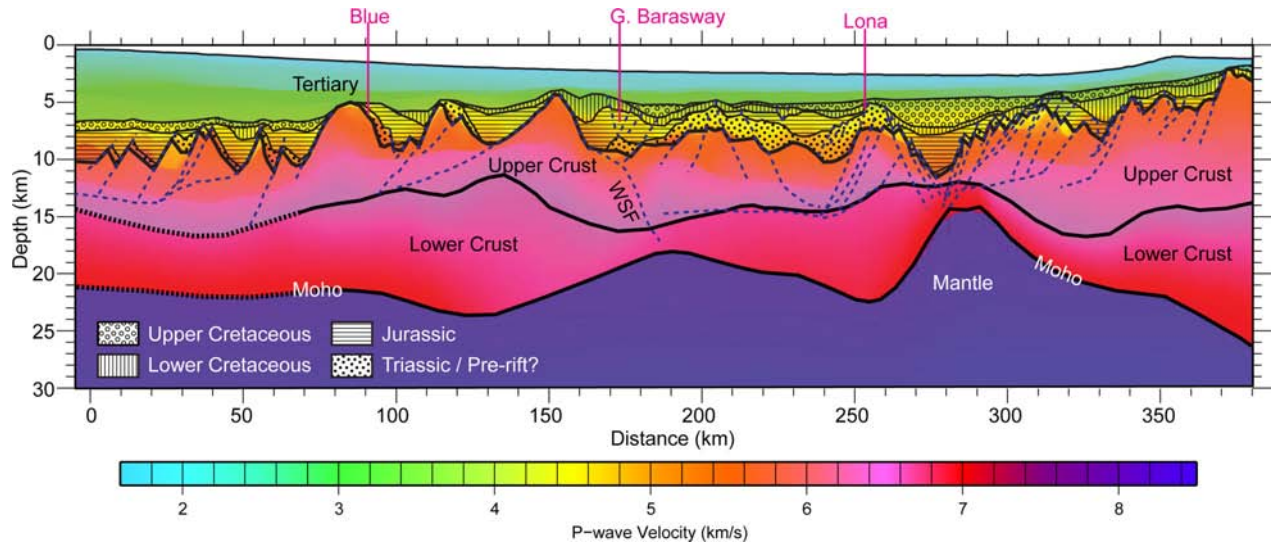
Figure 15. Geological interpretation of depth section Or0–122 (Fig. 14) by incorporating both the MCS reflectivity and the wide-angle velocity model (colour map). Dashed blue lines are interpreted faults responsible for upper crustal thinning.

Central Orphan High into the East Orphan Basin (Figs 2 and 9a). According to our combined interpretation based on relating seismic velocity with borehole data, the deepest sediment, Layer S7 with velocities >4 km s^{-1}, is consistent with a Jurassic age. This interpretation indicates that the Jurassic layer S7 continues into the West Orphan Basin (Fig. 15), suggesting an earlier age of rifting than previously proposed for this sub-basin (Enachescu *et al.* 2005). Note that sediment velocities for distances 55–75 km are as well constrained as those to the east (Fig. 9b). Such a re-interpretation is also consistent with the MCS data (Fig. 14b), where layer S7 generally coincides with a highly tectonized sequence above basement.

A deeper velocity layer (S8 at distances 190–270 km) is also observed as a similarly perturbed layer in the MCS data (Fig. 14a). It is possible that this layer may also extend into the deep sedimentary basin to the east (270–285 km), where a deep layer within the narrowest part of the basin (Fig. 15) would not be constrained by our velocity model. A roughly corresponding layer, extending throughout the East Orphan Basin (i.e. east of the WSF), has previously been interpreted as Triassic (Fig. 2a; Enachescu *et al.* 2005) although it has never been drilled. Note, however, that in their interpretation, the Triassic layer extends to a greater depth at distances 225–250 km, corresponding to the dipping reflections in the MCS profile, where our velocity model, in contrast, contains layers C1–C2 with much greater velocities (5.5–6.5 km s^{-1}) that we interpret as crust (Figs 14 and 15). Based on observations of tilted layering in the MCS section (Fig. 14), a thin layer of Triassic or pre-rift sediment is also interpreted as capping parts of the basement top within the western sub-basin (Fig. 15). These small zones of sediment are, however, not resolvable in the velocity model.

The wells Baccalieu I-78 and Mizzen L-11 (Fig. 1) are not used since they are farther away from our profile than the three wells mentioned above. They are also located within the Flemish Pass where large out-of-plane structural variations typical of large fault blocks are expected (Fig. 9a) and, therefore, do not justify a long distance projection onto the profile for comparison.

6.3 Crustal thinning

The top basement, mid-crustal boundaries and Moho in our velocity model are all much better constrained with the use of denser wide-

angle data than they are for typical wide-angle profiles (Watremez *et al.* 2015). These boundaries offer important, additional information for the interpretation of reflections observed in the MCS profile (Fig. 14). In particular, this well-constrained crustal model allows us to analyse both the whole crustal thinning and its partition into individual crustal layers by calculating the respective stretching factors,

$$\beta = h_\mathrm{o}/h(x), \tag{1}$$

where h_o is the unrifted thickness and $h(x)$ is the thickness at lateral position x; and their corresponding thinning factors,

$$\gamma = 1 - 1/\beta \tag{2}$$

(Fig. 16). Both β and γ values increase as extension thins the crust, although their differing transformations produce different patterns. β values become very large when the crust thins over ~60 per cent ($\beta > 3$; $\gamma > 0.6$), while γ values increase more rapidly during initial thinning of 0–50 per cent ($\beta = 1$–2; $\gamma = 0$–0.5).

Our three-layered crustal model based on modelled seismic velocities provides a seismic signature for the Orphan Basin crust and can be helpful in identifying the crustal province to which it belongs (i.e. Avalon; Hall *et al.* 1998). However, such detailed layering may be too complex for studying crustal thinning that focuses more on differences in large scale composition or rheology. Therefore, we sum layers C1 and C2 to represent the upper crust, while the single layer C3 represents the lower crust. This partition is chosen since it conforms best with changes in reflectivity between upper and lower crust observed in the MCS profile and since faults appear to terminate near to the top of layer C3 (Figs 14 and 15). This supports the interpretation of a brittle upper crust and a ductile lower crust (Gouiza *et al.* 2015). Full upper and lower crustal thicknesses of 12 and 22 km, respectively, are estimated according to their maximum thicknesses in the gravity model which extends further eastward (Fig. 13). For a homogeneous pure shear stretching model (e.g. McKenzie 1978), the two crustal layers should change their thicknesses uniformly, in contrast to DDS where changes in their thicknesses are non-uniform. Differences between the darker shade and the lighter shade blue or red curves in Figs 16(b) and (d), therefore, represent the degree of the DDS based on RAYINVR or Tomo2D modelling results, respectively. For such a comparison,
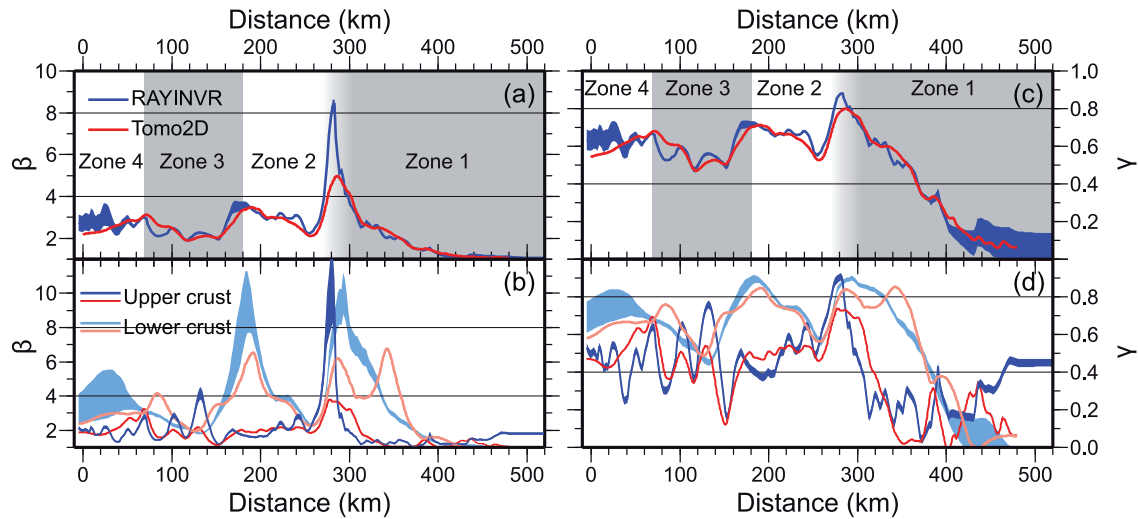
Figure 16. Crustal extension (β) and crustal thinning (γ) factors calculated from the RAYINVR layered model (this paper) and comparison with those from the Tomo2D model (Watremez *et al.* 2015). A full crustal thickness of 34 km is assumed. Estimated full upper and lower crustal thicknesses for the RAYINVR model are 12 and 22 km, respectively. Zones are the same as in Fig. 3. Uncertainties in β and γ are shown by the thicknesses of lines for the RAYINVR model. (a) Whole crustal extension factor (β_C). (b) Same as Fig. 16(a) except that factors are divided into upper and the lower crustal partitions (β_{UC}, β_{LC}). (c) Total crustal thinning factor (γ_C). (d) Upper and lower crustal thinning factors (γ_{UC}, γ_{LC}).

it is also important to consider the uncertainties in the β and γ values (Fig. 16) resulting from uncertainties in the depth to the Moho, the mid-crustal and the top basement boundaries as deduced in Section 4.3.

6.3.1 Lateral variation

The general pattern of whole crustal thinning (β_C, γ_C; Figs 16a and c) is very consistent between the Tomo2d and RAYINVR velocity models, suggesting that the modelling procedure does not influence detailed zonal interpretations concerning whole crustal thinning. Despite larger differences in upper (γ_{UC}) and lower crustal thinning (γ_{LC}) computed using the results from the two velocity modelling methods, DDS is clearly evidenced even after taking uncertainties into account. For simplicity, we only discuss the crustal thinning according to the layered model.

Within Zone 1, while the whole crustal β_C factor increases from 1 to $\sim$4 (γ_C from 0 to $\sim$0.8) for model distances 300–420 km (Figs 16a and c), the majority of this crustal thinning occurs within the lower crust (Figs 16b and d). At distance 280 km, extreme hyperextension is represented by a sharp spike in β_C (maximum $\sim$ 8.5; Fig. 16a). The hyperextension in the upper crust ($\beta_{UC} \sim 10.5$) is offset to the west by $\sim$20 km from that of the lower crust ($\beta_{LC} \sim 10.5$; Figs 16b and d). A westward dipping detachment is interpreted which results in a $\sim$9 km westward offset between the centre of the deep sedimentary basin at 278 km and the shallowest Moho at $\sim$287 km (Fig. 15).

In contrast to the boundary between Zones 1 and 2, the β_C within Zones 2–4 only varies slightly between 2 and 3.5 ($\gamma_C = 0.5$–0.7) with local peaks at $\sim$70 and $\sim$180 km, corresponding to the zonal boundaries (Fig. 16a). However, lower crustal thinning is much more variable within these zones and contrasts markedly with the relatively constant upper crustal thinning. The most dramatic difference is observed at distances 150–250 km. The peak of this difference at $\sim$180 km distance corresponds to the WSF, which appears to cut into the lower crust (Fig. 14a). The fault may continue through the lower crust, although its reflected amplitude may have been weak-

ened by interference from other reflections near or at the Moho. Note that velocities also do not appear to change across the fault (Fig. 9a). This smoothing can be caused by a decrease in velocities due to the presence of the fault and by spatial smoothing due to the modelling process.

The velocity structures in the lower crust within Zones 2 and 3 are not typical of perturbations caused by a single detachment fault (Fig. 9a). Velocities of 6.7–6.9 km s^{-1} are missing in the lower crust within Zone 3, resulting from a large amount of thinning at the bottom of the lower crust. To the east of the WSF (Zone 2), there is a thick region with velocities of 6.7–6.9 km s^{-1}, which may match with their deficit in Zone 3. However, this correspondence would be inconsistent with a simple eastward dipping fault which can only produce offsets in velocity contours instead of their complete removal. Furthermore, a much larger heave along the fault than observed is required to thin the $\sim$22 km thick lower crust to $\sim$2 km. Therefore, an additional process of ductile flow within the lower crust is needed to explain the observations. The ductile flow could be along a horizontal décollement in the middle of the lower crust within Zone 3 and at the top of the lower crust in Zone 2. In this interpretation, the upper part and the lower part of the lower crust within Zones 2 and 3, respectively, were squeezed out as the two zones extended along the décollement. Another unusual phenomenon is that velocity contours dip towards the Moho, unlike the more typical pattern observed for thinned crust such as at distances 270–370 km (Fig. 9a). This would require outflowing of lower crustal material away from the necking zone (distances 170–200 km) towards the Moho. Alternatively, the pre-rift structure of the crust may be more complex than our simplified model with three laterally homogeneous layers. Note that there is also a deficit in velocities of 6.9–7.1 km s^{-1} within both Zone 2 and 3.

The Central Orphan High has previously been interpreted as an initial H-block between the Bonavista Platform and Flemish Cap (Péron-Pinvidic & Manatschal 2010) using the velocity model of Chian *et al.* (2001). Such an H-block is defined as a large piece of mostly upper crust trapped between two major conjugate shear zones underpinning the H-block (Lavier & Manatschal 2006). Our model (Fig. 13) and fault interpretation (Fig. 15) do not, however,
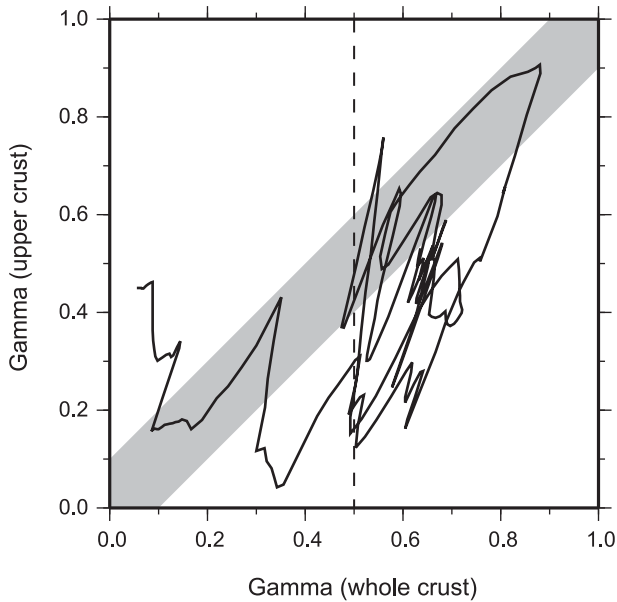
Figure 17. Trajectory of total crustal thinning (γ_C) versus upper crustal thinning (γ_{UC}) calculated every 2 km along the layered velocity model. Grey zone represents area with equal upper and total crustal thinning with an error of ± 0.1.

support this interpretation for two reasons. First, our model does not show a single thickened zone of crust towards the centre of the basin as proposed by the H-block model (Péron-Pinvidic & Manatschal 2010). Second, the WSF, which is the most prominent crustal scale fault in the basin, dips away from the centre of the basin (Fig. 15).

6.3.2 Mass balance of upper and lower crusts

In Fig. 17, we further consider the nature of DDS by plotting the upper crustal thinning factor (γ_{UC}) versus total γ_C along the layered velocity model. The ratios shown predominantly fall below the trend of no apparent DDS (i.e. $\gamma_{UC} = \gamma_C$) and demonstrate an apparent deficit in upper crustal thinning relative to lower crustal thinning over most of the profile. Such a deficit conflicts with an analysis of other North Atlantic margin profiles by Reston (2009), who showed that the average of these profiles did not indicate the existence of significant DDS. However, the older refraction results with standard shot-receiver geometries have much poorer resolution than our profile. In addition, many of these profiles traverse margins that exhibit rapid thinning seaward of the hinge zone. The nature of crustal thinning over this region is generally not very well constrained due to a limited coverage of diving rays (e.g. Lau *et al.* 2006; Gerlings *et al.* 2011). Thus, values of γ_{UC} versus γ_C are dominated by regions further seaward, over highly stretched crust ($\gamma_C > 0.5$). In these regions, crustal velocity-versus-depth values are not very well constrained due to the very few observations of first arrivals from diving rays in thin layers with high velocity gradients. In contrast, the OBWAVE profile extends over a crustal section with a greater continuity of γ_C values and lower crustal velocity gradients, except in a few regions of the most highly thinned crust.

The result of the apparent DDS along our profile leads to a deficit in the thickness of the lower crust, although this deficit is not large when considered as a percentage of the lower crustal section. Note that since both the gamma and the beta factors of the upper and lower crust are normalized by their respective full crustal thicknesses, they do not represent an absolute volume for

comparison and so can sometimes give a false impression of mass imbalance when DDS occurs. In our case, by summing the crustal units along the complete profile and comparing to the pre-rift crust of Flemish Cap, we determine that the ratio of rifted to original lower crust is ∼93 per cent. For an original lower crustal thickness of 22 km for Flemish Cap, this only produces a deficit of ∼1.5 km.

Such an apparent discrepancy can be largely accounted for by our estimated uncertainties in the depths of Moho (Fig. A2), mid-crustal (± 250 m) and basement (± 50 m) boundaries. Also, it could easily be explained if the velocities of the uppermost lower crust are reduced by faulting during extension, thus invalidating our use of a specific velocity to define the boundary between the upper and lower crust. Shallow drilling of basement highs on the margin of Iberia have sampled some lower crustal rock compositions in regions with lower modelled velocities (Whitmarsh *et al.* 2000), although these results come from complex environments with highly extended crust mixed with serpentinized upper mantle. More complete confirmation requires deep drilling into rifted crust at lower extension factors which is not feasible at present. The possibility of 3-D effects (i.e. movement of crust in and out of the 2-D section) might also be important in some instances. However, in contrast to the observed 3-D crustal geometries south of Galicia Bank (Péron-Pinvidic *et al.* 2007), the OBWAVE profile across Orphan Basin crosses primarily 2-D structures (Enachescu *et al.* 2005).

In summary, our analysis of the OBWAVE velocity profile suggests that an apparent DDS exists but does not result in a large amount of missing lower crust. Such a small lower crustal deficit might be explained by changing velocities at the boundary between the upper and lower crust due to complex faulting. This result does not explain the wide-spread discrepancy at most non-volcanic margins between fault-controlled extension and total crustal thinning (Reston 2007). A comparison of the MCS profile and velocity model (Fig. 14) indicates that the boundary between the upper and lower crust in the velocity model corresponds to a transition in reflectivity in which faulting is primarily limited to the upper crust. This observation suggests that the lower crust extends by non-rigid mechanisms, most probably by ductile shear, except for areas with extreme thinning (i.e. $\beta > 5$).

6.4 Regional comparison

Based on a plate reconstruction of the North Atlantic to M0 time (Louden *et al.* 2004), Rockall Trough, Porcupine Bank and Porcupine Basin are located in a conjugate position to the West Orphan Basin, the Central Orphan High and the East Orphan Basin, respectively (Fig. 18). Furthermore, the general strike of Rockall Trough and Porcupine Basin lie subparallel to the two major sub-basins of West and East Orphan Basins as defined by their basement depths. Results from wells (e.g. Shannon *et al.* 2007) indicate Jurassic ages for the opening of the Porcupine and Erris Basins (eastern edge of Rockall Trough), similar to those from wells in Orphan Basin (Fig. 10). Thus, it has previously been suggested that these basins developed together as part of a complex rift system extending from the Jeanne d'Arc Basin in the south to the inner Voring and possibly the Bjornoya basins west of Norway in the north (Lundin & Doré 2011).

In Fig. 19, we compare crustal sections for these basins determined from seismic velocity and gravity models (Morewood *et al.* 2005; O'Reilly *et al.* 2006). Each of the basins is asymmetrical and the two systems across the Atlantic share the same juxtaposition of a narrower eastern zone versus a wider western zone of hyperextended crust (<10 km). This further supports a connection
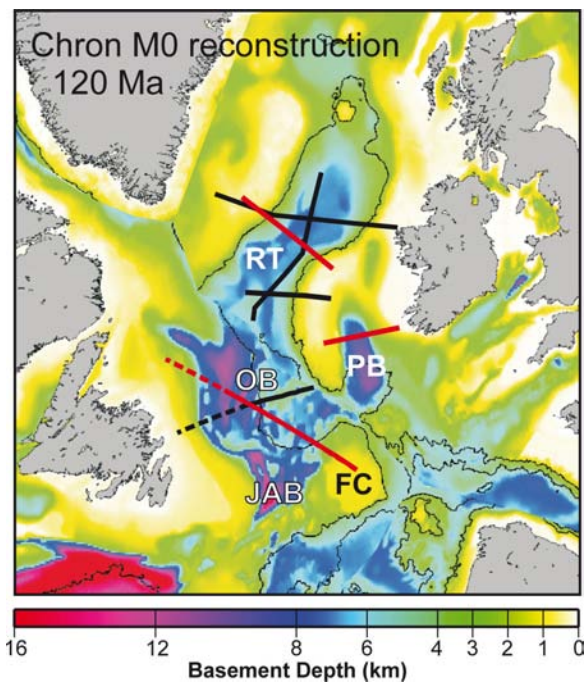
Figure 18. Plate reconstruction to Chron M0 showing basement depths (in colour scale) for the North America, northern Europe and Greenland margins (modified from Louden *et al.* 2004). Black thin lines are modern bathymetric contours (2000 and 4000 m) and shorelines. Red lines are cross sections shown in Fig. 19; thick black lines are other regional wide-angle OBS profiles. RT, Rockall Trough; PB, Porcupine Basin; OB, Orphan Basin; JAB, Jeanne d'Arc Basin; FC, Flemish Cap.

between the Rockall Trough and West Orphan Basins and between the Porcupine Basin and East Orphan Basins during rifting. However, we note that the basement structure for Orphan Basin is much more complex as the crustal block (Zones 2 and 3) that connects the two sub-basins is also thinned. Another difference is that the West and East Orphan Basins are narrower than the Rockall Trough and Porcupine Basin counterparts.

Finally, a substantial difference between structures across the conjugate systems is the evidence of partially serpentinized mantle in Rockall Trough and Porcupine Basin, based on uppermost mantle velocities of 7.2–7.6 km s^{-1} that are observed within the basins. The concept of crustal hyperextension has been developed (e.g. Lundin & Doré 2011; Pérez-Gussinyé 2012) from the rheological model of Pérez-Gussinyé & Reston (2001) to describe a threshold amount of extension beyond which the whole crust becomes brittle, allowing water to penetrate through the crust and serpentinize the mantle. While this effect is confirmed by seismic models of reduced mantle *P*-wave velocities (<8.0 km s^{-1}) where such criteria is met (e.g. Lau *et al.* 2006), some exceptions are also observed (e.g. van Avendonk *et al.* 2006). Following the methodology of Pérez-Gussinyé & Reston (2001), Reston (2009) predicts that the whole crust becomes brittle in Porcupine Basin and Rockall Trough when $\beta > 3.0$–3.3. This situation would allow water to penetrate into and partially serpentinize the upper mantle in areas where crustal thicknesses are less than ~10 km, in agreement with the seismic models (Figs 19a and b).

A similar transition for Orphan Basin would suggest that partially serpentinized mantle should also exist beneath the West and East Orphan basins (Fig. 19c). In contrast, we have presented strong evidence from both seismic and gravity models of normal mantle velocity and density beneath the East Orphan Basin. The absence

of serpentinization can perhaps be explained by the restricted size of the basin and its location adjacent to Flemish Cap. This would permit a larger supply of sediment to cover the basement early during its extension than on the conjugate system. Such a cover would inhibit the flow of water into the crust and thus leave the mantle intact. A similar situation may also explain the presence of normal mantle velocity beneath thinned crust on the FLAME profile in the section immediately east of Flemish Cap (Gerlings *et al.* 2011). However, this contradicts with the interpretation of only thin layers of Jurassic and Triassic sediment within the basin (Fig. 2; Enachescu *et al.* 2005).

For the West Orphan Basin, our structural constraints are based primarily on gravity modelling with the assumption that the densities of the various layers, including the mantle, remain constant. A lower mantle density due to partial serpentinization could be allowed beneath the West Orphan Basin if the crust is thinned slightly in order to produce the same total density column. The same situation exists for the previous profile of Chian *et al.* (2001), which also lacked seismic control west of the Blue H-28 well (Fig. 1). Thus, additional wide-angle seismic measurements are necessary in order to determine if the mantle is serpentinized beneath the West Orphan Basin.

7 CONCLUSIONS

We have developed a 2-D layered model across the full width of the Orphan Basin, from Flemish Cap to the Bonavista Platform, with the eastern 500 km portion constrained by modelling of high-resolution wide-angle seismic data and the western 200 km portion extended by modelling of satellite gravity data. A coincident MCS profile, well data and basement depths from previous studies were also used as constraints. Our results support the following conclusions:

(1) The layered velocity model in general agrees quite well with the smooth tomographic Tomo2D model presented by Watremez *et al.* (2015). However, the layered model includes velocity discontinuities that enable a more detailed delineation of sediment and crustal layers and, therefore, a better comparison with the coincident MCS profile.

(2) The syn-rift Jurassic sediment (velocities > 4 km s^{-1}) is interpreted to extend fully across the Orphan Basin from the eastern into the western sub-basins, suggesting an earlier rifting age (Jurassic or earlier) than previously determined. The BT discontinuity marks a major change in velocity (difference ~0.5–1 km s^{-1}) consistent with the Blue H-28 and Lona O-55 wells, but deeper (depth = 4.8 km) than previously interpreted at the Great Barasway F-66 well (3.9 km).

(3) Variations in crustal thicknesses within the basin are highly complex, with a minimum and maximum thickness of 4 and 32 km, respectively. A deep trough with hyperextended crust (thickness <10 km) is observed at each side of the eastern and western sub-basins. The zone of hyperextended crust is wider in the western than it is in the eastern sub-basin; and the change in Moho depth is narrower in the western than it is in the eastern sub-basin, giving an asymmetrical shape across the full rift.

(4) Two distinctive zones on both sides of the WSF, near the centre of the basin (model distances 70–270 km), contain thicker crust (>10 km) with complex structures. The relatively muted topography (depths of 7–10 km) in the eastern contrasts with the three major basement highs (depths of 4–10 km) in the western zone. Their velocity structures in the lower crust do not resemble that of the thinned crust beneath Flemish Pass. Since the higher velocities
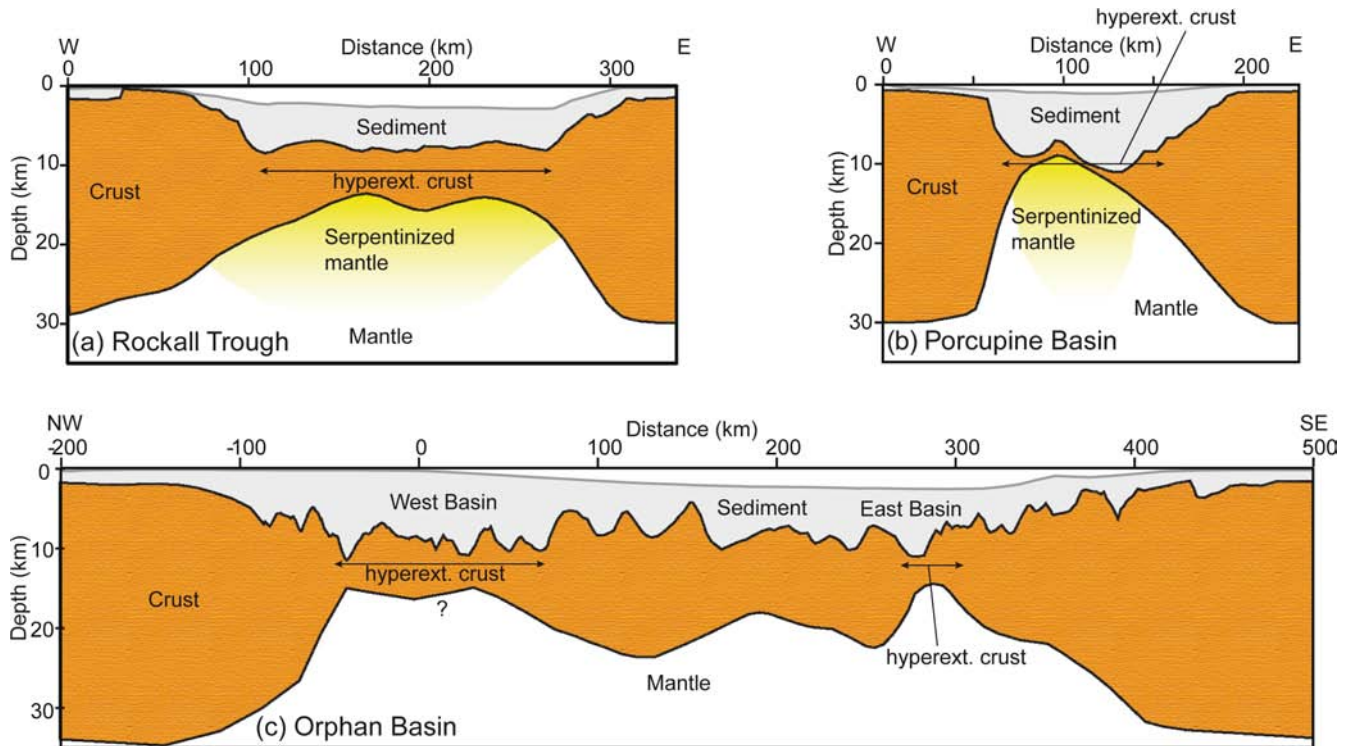
Figure 19. Structural comparison between the Orphan Basin and its European counterparts. Structures are constrained by dense wide-angle data, except for the western end of Orphan Basin which is determined by gravity modelling (Fig. 13). Zones with crustal thicknesses <10 km are marked as hyperextended crust. (a) Rockall Trough (Morewood *et al.* 2005). (b) Porcupine Basin (O'Reilly *et al.* 2006). (c) Orphan Basin (this paper). Question mark represents potential existence of serpentinized mantle.

$(6.7–7.0 \text{ km s}^{-1})$ within eastern zone and the lower velocities $(6.5–6.9 \text{ km s}^{-1})$ in the western zone cannot be explained by displacement along the WSF, this may suggest lateral ductile flow within the lower crust, resulting in DDS. A deep horizontal décollement to the west and a shallow one to the east of the WSF are possible.

(5) Evidence for DDS is also clearly documented by discrepancies between upper crustal thinning (γ_{UC}) and lower crustal thinning (γ_{LC}) as defined in the velocity model. However, the presence of DDS only produces a small deficit (∼7 per cent or 1.5 km) in the lower crustal section, which can be accounted for by changes in velocity of the lower crust due to faulting during crustal thinning as observed in the MCS data.

(6) Reconstruction of the North Atlantic at M0 time indicates a complex connection between Rockall Trough and the West Orphan Basin, Porcupine Bank and the East Orphan Basin, and the Central Orphan High and Porcupine Bank. Similarity in crustal structure between them (a wider hyperextended western basin is paired with a narrower eastern basin by a middle zone of thicker crust) further supports this connection.

(7) Unlike the Rockall and Porcupine Basins, no evidence for partial serpentinization of the upper mantle is observed beneath the East Orphan Basin where crust should have become entirely brittle. One possible scenario may be that this narrow zone (∼30 km wide) of potentially brittle crust has been covered by syn-rift sediment that inhibited the flow of water down the faults.

ACKNOWLEDGEMENTS

REFERENCES

Chian, D., Marillier, F., Hall, J. & Quinlan, G., 1998. An improved velocity model for the crust and upper mantle along the central mobile belt of the Newfoundland Appalachian orogen and its offshore extension, *Can. J. Earth Sci.,* **35**(11), 1238–1251.

Chian, D., Reid, I.D. & Jackson, H.R., 2001. Crustal structure beneath Orphan Basin and implications for nonvolcanic continental rifting, *J. geophys. Res.,* **106**(B6), 10 923–10 940.

Davis, M. & Kusznir, N.J., 2004. Depth-dependent lithospheric stretching at rifted continental margins, in *Rheology and Deformation of the Lithosphere at Continental Margins,* pp. 92–136, eds Karner, G.D., Taylor, B., Driscoll, N.W. & Kohlstedt, D.L., Columbia University Press.

Driscoll, N.W. & Karner, G.D., 1998. Lower crustal extension across the Northern Carnarvon basin, Australia: evidence for an eastward dipping detachment, *J. geophys. Res.,* **103**(B3), 4975–4991.

Enachescu, M. *et al.*, 2005. Evolution and petroleum potential of Orphan Basin, offshore newfoundland, and its relation to the movement and rotation of Flemish Cap Based on Plate Kinematics of the North Atlantic, in *Petroleum Systems of Divergent Continental Margin Basins: 25th Annual,* Vol. 25, pp. 75–131, Society of Economic Paleontologies and Mineralogists.

Ford, J.H. & Johnston, P.F., 2003. *Biostratigraphic Analysis - Texaco Shell et al. BLUE H-28, 2070 to 6103 m. TD. Orphan Basin, East Coast Offshore Newfoundland,* Ford Biostratigraphic Services.

Gerlings, J., Louden, K.E. & Jackson, H.R., 2011. Crustal structure of the Flemish Cap Continental Margin (eastern Canada): an analysis of a seismic refraction profile, *Geophys. J. Int.,* **185**(1), 30–48.

Gouiza, M., Hall, J. & Bertotti, G., 2015. Rifting and pre-rift lithosphere variability in the Orphan Basin, Newfoundland margin, Eastern Canada, *Basin Research*, **27**, 367–386.

Hall, J., Marillier, F. & Dehler, S., 1998. Geophysical studies of the structure of the Appalachian orogen in the Atlantic borderlands of Canada, *Can. J. Earth Sci.,* **35**(11), 1205–1221.

Keen, C.E. & Barrett, D.L., 1981. Thinned and subsided continental crust on the rifted margin of Eastern Canada: crustal structure, thermal evolution and subsidence history, *Geophys. J. R. astr. Soc.,* **65**(2), 443–465.

Kusznir, N.J. & Karner, G.D., 2007. Continental lithospheric thinning and breakup in response to upwelling divergent mantle flow: application to the Woodlark, Newfoundland and Iberia margins, *Geological Society, London, Special Publications,* **282**(1), 389–419.

Lau, K.W.H., Louden, K.E., Funck, T., Tucholke, B.E., Holbrook, W.S., Hopper, J.R. & Larsen, H.C., 2006. Crustal structure across the Grand Banks–Newfoundland Basin Continental Margin – I. Results from a seismic refraction profile, *Geophys. J. Int.,* **167**(1), 127–156.

Lavier, L.L. & Manatschal, G., 2006. A mechanism to thin the continental lithosphere at magma-poor margins, *Nature,* **440**(7082), 324–328.

Louden, K.E., Tucholke, B.E. & Oakey, G.N., 2004. Regional anomalies of sediment thickness, basement depth and isostatic crustal thickness in the North Atlantic Ocean, *Earth planet. Sci. Lett.,* **224**(1–2), 193–211.

Lundin, E.R. & Doré, A.G., 2011. Hyperextension, serpentinization, and weakening: a new paradigm for rifted margin compressional deformation, *Geology,* **39**(4), 347–350.

McKenzie, D., 1978. Some remarks on the development of sedimentary basins, *Earth planet. Sci. Lett.,* **40**, 25–32.

Morewood, N.C., Mackenzie, G.D., Shannon, P.M., O'Reilly, B.M., Readman, P.W. & Makris, J., 2005. The crustal structure and regional development of the Irish Atlantic margin region, *Geological Society, London, Petroleum Geology Conference series,* **6**, 1023–1033.

O'Reilly, B.M., Hauser, F., Ravaut, C., Shannon, P.M. & Readman, P.W., 2006. Crustal thinning, mantle exhumation and serpentinization in the Porcupine Basin, offshore Ireland: evidence from wide-angle seismic data, *J. geol. Soc. Lond.,* **163**(5), 775–787.

Pérez-Gussinyé, M., 2012. A tectonic model for hyperextension at magma-poor rifted margins: an example from the West Iberia–Newfoundland conjugate margins, *Geological Society, London, Special Publications,* **369,** doi:10.1144/SP369.19.

Pérez-Gussinyé, M. & Reston, T.J., 2001. Rheological evolution during extension at nonvolcanic rifted margins: onset of serpentinization and development of detachments leading to continental breakup, *J. geophys. Res.,* **106**(B3), 3961–3975.

Péron-Pinvidic, G. & Manatschal, G., 2010. From microcontinents to extensional allochthons: witnesses of how continents rift and break apart?, *Petroleum Geoscience,* **16**(3), 189–197.

Péron-Pinvidic, G., Manatschal, G., Minshull, T.A. & Sawyer, D.S., 2007. Tectonosedimentary evolution of the deep Iberia-Newfoundland margins: evidence for a complex breakup history, *Tectonics,* **26**(2), doi:10.1029/2006TC001970.

Reston, T. J., 2007. Extension discrepancy at North Atlantic nonvolcanic rifted margins: depth-dependent stretching or unrecognized faulting?, *Geology,* **35**(4), 367–370.

Reston, T.J., 2009. The structure, evolution and symmetry of the magma-poor rifted margins of the North and Central Atlantic: a synthesis, *Tectonophysics,* **468**(1–4), 6–27.

Sandwell, D.T. & Smith, W.H.F., 2009. Global marine gravity from retracked Geosat and ERS-1 altimetry: ridge segmentation versus spreading rate, *J. geophys. Res.,* **114**(B1), doi:10.1029/2008JB006008.

Shannon, P.M., McDonnell, A. & Bailey, W.R., 2007. The evolution of the Porcupine and Rockall basins, offshore Ireland: the geological template for carbonate mound development, *International Journal of Earth Sciences,* **96**(1), 21–35.

Sibuet, J.-C., Srivastava, S.P., Enachescu, M.E. & Karner, G.D., 2007. Early Cretaceous motion of Flemish Cap with respect to North America: implications on the formation of Orphan Basin and SE Flemish Cap–Galicia Bank conjugate margins, in *Imaging, Mapping and Modelling Continental Lithosphere Extension and Breakup,* Vol. 282, pp. 63–76, eds Karner, G.D., Manatschal, G. & Pinheiro, L.M., Geological Society, Special Publications.

Skogseid, J., 2010. *The Orphan Basin—A Key to Understanding the Kinematic Linkage between North and NE Atlantic Mesozoic Rifting*, Vol. 2, pp. 13–23, Statoil ASA.

Srivastava, S.P. & Verhoef, J., 1992. Evolution of Mesozoic sedimentary basins around the North Central Atlantic: a preliminary plate kinematic solution, *Geological Society, London, Special Publications,* **62**(1), 397–420.

Talwani, M., Worzel, J.L. & Landisman, M., 1959. Rapid gravity computations for two-dimensional bodies with application to the Mendocino submarine fracture zone, *J. geophys. Res.,* **64**(1), 49–59.

Van Avendonk, H.J.A., Holbrook, W.S., Nunes, G.T., Shillington, D.J., Tucholke, B.E., Louden, K.E., Larsen, H.C. & Hopper, J.R., 2006. Seismic velocity structure of the rifted margin of the eastern Grand Banks of Newfoundland, Canada, *J. geophys. Res.,* **111**, B11404, doi:10.1029/2005JB004156.

Watremez, L., Lau, K.W.H., Nedimović, M.R. & Louden, K.E., 2015. Traveltime tomography of a dense wide-angle profile across Orphan Basin, *Geophysics,* **80**(3), B69–B82.

Welford, J.K., Shannon, P.M., O'Reilly, B.M. & Hall, J., 2012. Comparison of lithosphere structure across the Orphan Basin–Flemish Cap and Irish Atlantic conjugate continental margins from constrained 3D gravity inversions, *J. geol. Soc.,* **169**(4), 405–420.

Wessel, P. & Smith, W.H.F., 1998. New, improved version of generic mapping tools released, *EOS, Trans. Am. geophys. Un.,* **79**(47), 579–579.

White, N. & McKenzie, D., 1988. Formation of the "steer's head" geometry of sedimentary basins by differential stretching of the crust and mantle, *Geology,* **16**(3), 250–253.

Whitmarsh, R.B., Dean, S.M., Minshull, T.A. & Tompkins, M., 2000. Tectonic implications of exposure of lower continental crust beneath the Iberia Abyssal Plain, Northeast Atlantic Ocean: geophysical evidence, *Tectonics,* **19**, 919–942.

Won, I.J. & Bevis, M., 1987. Computing the gravitational and magnetic anomalies due to a polygon; algorithms and Fortran subroutines, *Geophysics,* **52**(2), 232–238

Zelt, C.A. & Smith, R.B., 1992. Seismic traveltime inversion for 2–D crustal velocity structure, *Geophys. J. Int.,* **108,** 16–34.

APPENDIX : SUPPLEMENTARY FIGURES

Figs A1–A3 illustrate observations of both crustal and Moho reflections in the OBS data and their resolutions in the velocity models.
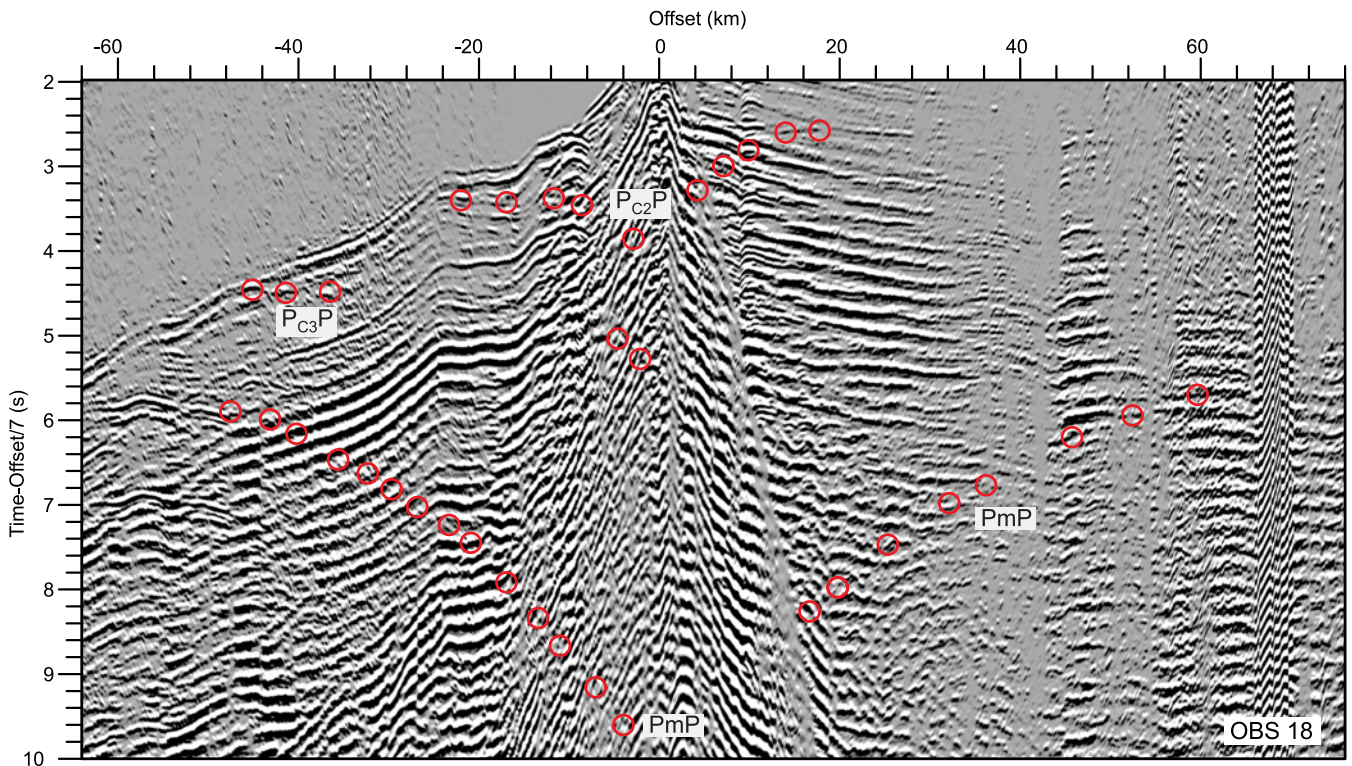

Figure A1. Vertical geophone data of OBS 18. Traveltime is reduced by 7 km s^{-1} relative to shot-receiver offsets. The data have been processed with minimum phase bandpass filtering, trace interpolation and dip filtering to enhance deep crustal and mantle signals and to attenuate the wrap-around noise. Red circles locate observed wide-angle mid-crustal and Moho reflections as labelled. See Table 1 for nomenclature of observed phases.
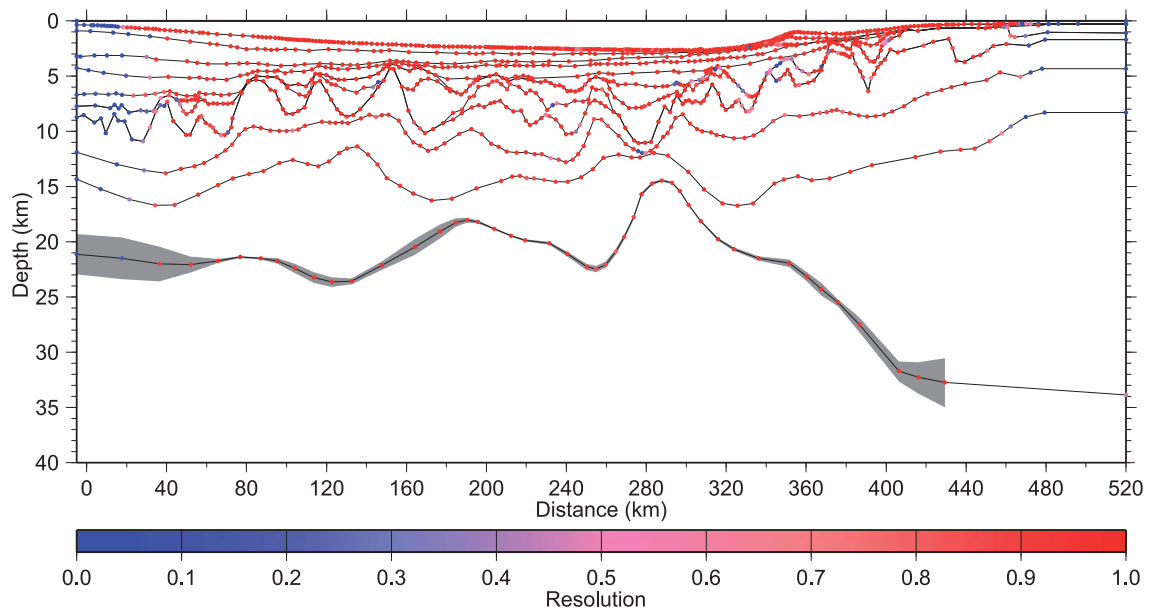

Figure A2. Depth resolution of final *P*-wave velocity model boundaries. Velocity model layer boundaries are in black lines and depth nodes resolutions defined by colour scale. Shaded area represents standard deviations of inverted Moho by Watremez *et al.* (2015).
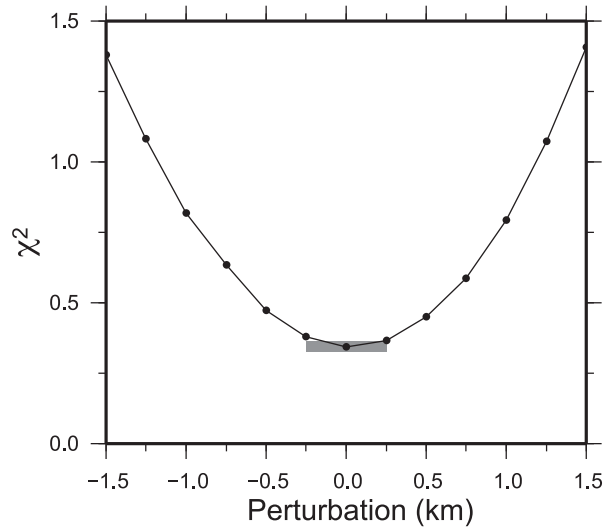
Figure A3. Chi-square (χ^2) as a function of vertical perturbations to nine depth nodes of the upper-to-lower crustal boundary for distances 155–220 km. The central five nodes were perturbed by the amount shown by the points in the figure and the two nodes at each side served as a linear taper. The OBS coverage of four progressively narrower ranges (52–72, 54–71, 56–69 and 58–67) chosen above the perturbed boundary was included in each set of perturbation analysis and the shown χ^2 values are the average of the four. Grey bar shows the uncertainty in the boundary depths based on the *f*-test using results from the OBS 56–69 run. Perturbations outside of this range yield models that are different from our final model at >98 per cent confidence. Note that we did not test perturbation smaller than 250 m.